3-8-2016

Orion's Veil. IV. H_2 Excitation and Geometry

N. P. Abel
University of Cincinnati - Clermont College

Gary J. Ferland
University of Kentucky, gary@uky.edu

C. R. O'Dell
Vanderbilt University

Thomas H. Troland
University of Kentucky, troland@pa.uky.edu

Orion's Veil. IV. H_2 Excitation and Geometry

Digital Object Identifier (DOI)
https://doi.org/10.3847/0004-637X/819/2/136

The Astrophysical Journal, 819:136 (18pp), 2016 March 10 doi:10.3847/0004-637X/819/2/136

ORION'S VEIL. IV. H_2 EXCITATION AND GEOMETRY

N. P. Abel[1], G. J. Ferland[2,3], C. R. O'Dell[4], and T. H. Troland[2]
[1] University of Cincinnati, Clermont College, MCGP Department, Batavia, OH 45103, USA; abelnp@ucmail.uc.edu
[2] University of Kentucky, Department of Physics and Astronomy, Lexington, KY 40506, USA; gary@pa.uky.edu, troland@pa.uky.edu
[3] School of Mathematics and Physics, Queen's University Belfast, Belfast BT7 1NN, Northern Ireland, UK
[4] Department of Physics and Astronomy, Vanderbilt University, Box 1807-B, Nashville, TN 37235, USA; cr.odell@vanderbilt.edu
Received 2015 August 22; accepted 2016 January 7; published 2016 March 8

ABSTRACT

The foreground Veil of material that lies in front of the Orion Nebula is the best studied sample of the interstellar medium because we know where it is located, how it is illuminated, and the balance of thermal and magnetic energy. In this work, we present high-resolution STIS observations toward the Trapezium, with the goal of better understanding the chemistry and geometry of the two primary Veil layers, along with ionized gas along the line of sight. The most complete characterization of the rotational/vibrational column densities of H_2 in the almost purely atomic components of the Veil are presented, including updates to the Cloudy model for H_2 formation on grain surfaces. The observed H_2 is found to correlate almost exclusively with Component B. The observed H_2, observations of CI, CI*, and CI**, and theoretical calculations using Cloudy allow us to place the tightest constraints yet on the distance, density, temperature, and other physical characteristics for each cloud component. We find the H_2 excitation spectrum observed in the Veil is incompatible with a recent study that argued that the Veil was quite close to the Trapezium. The nature of a layer of ionized gas lying between the Veil and the Trapezium is characterized through the emission and absorption lines it produces, which we find to be the blueshifted component observed in S III and P III absorption. We deduce that, within the next 30–60 thousand years, the blueshifted ionized layer and Component B will merge, which will subsequently merge with Component A in the next one million years.

Key words: ISM: molecules – magnetic fields – photon-dominated region (PDR)

1. INTRODUCTION

Orion's Veil is a series of atomic/ionized cloud components along the line of sight toward the Orion Nebula (Abel et al. 2004, 2006 and reference therein, henceforth A04 and A06). The Veil is the primary source of extinction toward M42, and is physically associated with the Orion environment. The physical association of the Veil with Orion, proximity to the ionizing stars of M42, known as the Trapezium, and the Veil's geometric similarities to diffuse clouds make it an ideal region to test physical processes in the ISM, with application to the physics and chemistry of PhotoDissociation Regions (PDRs) and the role of magnetic fields play in the energetics of the ISM and star-forming regions.

While the Veil extends across the brightest part of M42, known as the Huygens Region, this work will focus on the sightline toward the Trapezium. The UV/optical source provided by the Trapezium, along with the radio emission from M42, provides a strong background source for absorption studies of the Veil. Many of the UV/optical/radio absorption studies are reviewed in A04 and A06. Therefore we only summarize the most important observations here, and point the reader to the earlier literature for a more complete description.

H I absorption studies (van der Werf & Goss 1989; A06) show two cloud components, labeled A (at 23.4 km s^{-1}) and B (at 19.4 km s^{-1}).[5] These velocities, along with all velocities in this paper, will be reported as heliocentric, which is 18.1 km s^{-1} more positive than the velocity in the local standard rest frame (V_{LSR}). The superior spectral resolution provided by the H I data provides constraints on the kinetic temperature (through the linewidth) and the ratio of the atomic hydrogen column density ($N(H^0)$) to spin temperature (T_{spin}) characterizing the excitation of the 21 cm hyperfine structure. In addition, Zeeman splitting of the 21 cm line measured with the VLA provides information on the magnetic field strength in components A and B.

The UV/optical studies provide information on the dust and gas-phase abundances in the Veil. In the optical, extinction measurements across the Veil allow for a map of the extinction across the entirety of M42 (O'Dell & Yusef-Zadeh 2000). Toward the Trapezium, the ratio of total to selective extinction, $R_V = A_V/E(B-V)$ is between 5 and 5.5 (Bohlin & Savage 1981), significantly larger than the average ISM value of 3.1 and indicative of an environment with larger than average grains. UV data gives us information on the chemical abundances (Lykins et al. 2010) in each cloud component, and the total H I column density. UV absorption studies provide clear evidence of an ionized (H^+) component along the line of sight (which must lie between the Trapezium and atomic layers) through S III and P III absorption (henceforth this ionized component will be called the "Ionized Layer"). Of particular importance to this work is the low abundance of H_2 in the Veil, in the direction of the Trapezium (other, thicker portions of the Veil are seen in OH absorption and hence have much higher molecular abundances). Copernicus and *IUE* did not detect H_2, placing only upper limits on the total H_2 column density. A06, using archival STIS data, observed four H_2 lines in absorption, but only in highly excited states corresponding to $v = 3$, $J = 1$, 3. In addition, these measurements were pushing the limits of statistical significance given the signal-to-noise ratio (S/N) of the archival data and were not clearly associated with component A or B.

[5] In the introduction of A06, the velocities of A and B were mislabeled, an error which only occurred in the introduction and did not propagate through any of the results and conclusions drawn from A06.

In A04 and A06, the wealth of UV, radio, and optical data were combined with theoretical calculations in order to understand the physical conditions in each cloud component. Using the observational constraints on temperature, H_2 abundance, level of ionization, and the column densities of C^0 in the $J = 0$, 1, and 2 levels (henceforth CI, CI*, and CI**), our previous work determined the density and temperature in each cloud component. When combined with magnetic field measurements, we found component A is dominated by magnetic energy, and is not in energy equipartition. Equipartition is often assumed in the ISM, and is the likely final state for a long-term stable region of the ISM. The large number of high quality observables for the Veil, and the fact it is not in energy equilibrium, makes the Veil an ideal test bed to study the energy partitioning of the ISM and regions associated with star formation (the Veil does not itself have stars actively forming, but is associated physically with the Orion Complex). Additionally, we found the lack of H_2, despite the significant $N(H^0)$ column density of $10^{21.68\pm0.12}$ (Cartledge et al. 2001) is a result of the larger dust grains allowing more UV radiation through the Veil, and the Veil's close proximity to the Trapezium providing a large UV flux.

Despite the success of A04 and A06 in understanding the physical characteristics of the Veil, important questions remain unanswered. Of particular importance to this work, these include:

1. *The distance of component A and B to the Trapezium*. A06 applied the models developed in A04 using Cloudy (Ferland et al. 2013). However, A04 modeled the Veil as a single cloud. As a result, previous work could only determine an average distance to the Veil, and not determine the distance of each individual component to the Veil. We now know the column densities of many species for each 21 cm component through UV absorption measurements with STIS (both archival and those presented below) which puts tighter constraints on each cloud component. Recent work by van der Werf et al. (2013) place component B significantly closer to the Trapezium than A06, arguing based on geometric and dynamical considerations that component B must be (1) closer to the Trapezium than component A and (2) must be within 0.4 pc to the cluster. A better understanding of the distances between cloud components and the Trapezium would improve the chemical model of the Veil, better quantify the energy partitioning in the Veil, and allow us to develop a better model for the overall geometry of the Orion environment.
2. *The abundance of H_2 in the Veil*. Almost all clouds with the H^0 abundance observed in the Veil have orders of magnitude more H_2 (Savage et al. 1977). A06 showed it is possible to detect H_2 in the Veil, but the amount of H_2 was not well characterized. Is most of the H_2 in component A or component B? Given the low abundance of H_2, the H_2 in the Veil is likely not undergoing significant self-shielding, meaning the UV radiation field impingent upon the illuminated face of the Veil makes it through the side of the Veil facing Earth. A06 showed that the significant UV flux will lead to a highly excited environment where the H_2 levels are populated through radiative, as opposed to collisional, processes, with a larger fraction of the total H_2 column density residing in higher v, J levels than a classical PDR observed in the infrared. Recent theoretical work (Le Bourlot et al. 2012; Röllig et al. 2013) show, in regions which have not undergone self-shielding, that the H_2 formation rate on grains can be an order of magnitude higher than previously thought due to the Eley–Rideal mechanism. This process involves forming H_2 through a gas phase hydrogen atom coming in contact with a location on a grain which already possesses another hydrogen atom, and through chemisorption H_2 is formed (see also Le Bourlot et al. 2012; Röllig et al. 2013 for a description of Eley–Rideal). This results in increased heating of the atomic gas and increased abundances of v, J levels. The primary focus of previous work on the Eley–Rideal mechanism was on the effects on the H_2 and CO infrared emission spectrum for application to dense PDRs and molecular clouds. However, with the Veil, we have the opportunity to study the Eley–Rideal process in absorption. Understanding how the Eley–Rideal process affects the abundance of the rotational/vibrational levels in a well-characterized local environment through direct observation of the level populations in absorption will help refine models of H_2 formation used in understanding the emission-line spectrum in regions less spatially resolved.
3. *Characteristics of the Ionized Layer along the line of sight*. The presence of P III and S III ultraviolet absorption lines (A06) argues that there is an ionized gas layer between the observer and the Trapezium. These are in addition to the He I 3889 Å 2.1 km s^{-1} absorption line known to exist in all four Trapezium stars and at 2.9 km s^{-1} in the nearby Orion Nebula Cluster star θ^2 Ori A. In A06 the existence of a second ionized layer was posited and in Sections 3 and 6 we develop more completely the model for this layer.
4. In this work, we will present new observations and theoretical calculations designed to answer the bulleted items above. In Section 2, we discuss new high-resolution STIS observations toward the Trapezium, while Section 3 discusses our analysis of the foreground ionized layers. Section 4 describes the PDR simulations designed to provide refined physical conditions in each H I cloud component, and determine the distance of each component from the Trapezium. We then apply the model to the observations in Section 5, and describe our results and conclusions in Section 6.

2. OBSERVATIONS AND DATA REDUCTION

On February 6th, 2014 the *Hubble Space Telescope* was pointed toward θ^1 Ori B, one of the Trapezium stars of M42, as part of observing program 13310. We were allocated four orbits, spanning a total of 10,800 s of observing time. We used the STIS/E140H setting with a wavelength coverage between 1133 and 1335 Å for each orbit. Each orbit produced a single x1d spectra, which we then reprocessed using the latest version of IRAF (Tody 1993) by use of the x1d task. The edges of each spectral order are typically of lower quality, therefore we flagged these edges as bad pixels in the reprocessed x1d spectra and removed these pixels from the final extraction. The four reprocessed spectra were then averaged using the IRAF task splice. This allowed us create a single spectrum with a higher S/N than any of the four original spectra. Adjacent orders of

the E140H instrument contain some wavelength overlap. Splicing our spectra into a single spectrum therefore allowed us to average adjacent orders, improving the S/N. Overall, our single spectra produced the high S/N necessary to detect rotationally/vibrationally excited H_2 in absorption. The S/N of our co-added data exceeds 20 over the entire wavelength coverage of our spectra. Most importantly, beyond 1240 Å, the S/N often exceeds 100, and exceeds 50 in most regions between 1150 and 1200 Å. This far exceed the S/N of ~20–30 from the earlier 1172–1370 Å toward this sightline obtained in observing program 8273 (Cartledge et al. 2001). As we show in Table 3, this allows us to achieve, with 3σ confidence, detections of over twenty H_2 absorption lines just a few percent below the continuum at a spectral resolution of 2.5 km s^{-1}.

Given the final, co-added spectra, we proceeded to identify absorption features in the spectrum. Several databases were used in this endeavor. For atomic/ionic species, we used the Morton UV database (2003), along with the databases provided in the FITS6p UV profile-fitting package, described in Welty et al. (1999). This allowed us to eliminate many absorption features as belonging to atomic or ionic species. Many of the same transitions observed in Cartledge et al. (2001) and A06 are also observed in our spectrum, such as Kr I, Ni II, Ge II, and N I. Our current dataset does not add anything new to the analysis of these lines, therefore we only identified these species for purposes of eliminating all non-H_2 features. The one exception to this was the CI, CI*, and CI** absorption features, which were fully analyzed due to their temperature and density diagnostic capabilities.

Once all non-H_2 features were cataloged, we went through the spectrum and identified all absorption features which did not have an identification, using the well characterized velocity component structure for H I component A and B to Doppler-shift all observed wavelengths for comparison to the database. We compared the observed features to one of two databases, the H2ools website (McCandliss 2003) and the internal H_2 database in Cloudy (Ferland et al. 2013). In most cases, a match was found between a Doppler-shifted absorption feature and the H_2 databases. For those instances where there was more than one match, we eliminated those transitions which came $v > 5$, $J > 10$, as our previous modeling (A06) showed these levels should have a column density too low to detect even with our high S/N data. We also eliminated from the database all absorption features which, after measuring the equivalent width, predicted an H_2 column density greater than the limit allowed by Copernicus observations, $10^{17.55}$ cm^{-2} (Savage et al. 1977). This always left us with a single H_2 transition which, with high probability, is the cause of the observed absorption feature.

For all H_2 and carbon absorption features, equivalent widths and velocities were measured using IRAF. Once an absorption feature was identified, a region centered on the absorption feature was extracted using the scopy task. The continuum of the extracted region was fit using the continuum task. We marked locations on either side of the absorption feature during the fit, and constrained the continuum fit with those markings. The final fit was then used to produce a normalized spectrum. To compute errors in the measured equivalent widths and velocities, the rms was measured on either side of the absorption feature and then averaged. This average rms was then set as σ_0 in the splot error package, with nerrsample set to 100 and invgain = 0.

For H_2, we tried one and two component fits, however two component fits always led to one component being unreasonably broad, or the 2nd component in the fit showing emission. We found, for all H_2 lines, a single component fit worked well. For CI and CI*, a two component fit best fit the data for multiple transitions, while for CI** a single component fit worked best. As we will demonstrate in Section 5, the lack of a 2nd component for H_2 and CI** is a direct consequence of the different physical conditions in components A and B.

The final line identifications along with the measured equivalent widths, velocities, and 1σ errors are shown in Tables 1 and 2. All absorption features we analyzed are comfortably on the linear part of the curve-of-growth (COG), allowing us to measure equivalent widths without needing the b-value in the computing of column densities, using the equation:

$$N = \frac{1.13 \times 10^{17} W_\lambda}{\lambda^2 f} \quad (1)$$

where W_λ is the equivalent width (measured in mÅ), λ is the wavelength (measured in Å) and f is the oscillator strength. The earlier A06 dataset measured a CI** transition with a stronger oscillator strength, at a wavelength not covered by our current dataset. Therefore, Table 2 reports the value taken from A06 as the 2nd component for CI**. The reported errors are errors corresponding to fitting the continuum and equivalent width for the rms on either side of the spectral feature, and not associated with any potential errors arising in the atomic data (wavelength, oscillator strength. In addition, we sampled individual lines of the four original spectra, and computed errors to see how the errors computed individually statistically compared to the errors of the final, co-added spectra. For the 1283.11 Å H_2 line, the average equivalent width for the four individual spectra came to 2.1 mÅ +/− 0.19, comparable to the 1.8 mÅ ± 0.15 we found for the co-added spectra.

The measured equivalent widths and velocities for all H_2 features are presented in Table 1. Twenty-two H_2 absorption features were reliably detected (above 3σ), sampling twelve v, J levels. This far exceeds the four absorption lines reported in Abel et al. (2006). Table 3 also shows the computed column density for each absorption line (many of which are shown in Figure 1), using Equation (1). Figure 2 shows the normalized absorption profiles for 12 of the lines identified as H_2. Table 2 shows the same measurements for CI, CI*, and CI** along with the column densities computed using Equation (1). The CI, CI*, and CI** equivalent widths, velocities, and column densities are shown in Table 2.

The observational data show important trends. First, it is clear from the H_2 absorption profiles that nearly all of the H_2 is associated with component B (Figure 1). The velocities are almost always between 18 and 20 km s^{-1}, with only a single absorption feature, corresponding to $v = 1$, $J = 3$, having a velocity above 21 km s^{-1}. This level also has the highest column density, and therefore could potentially represent H_2 coming from both component A and B. However, multi-component fits to this line gave large errors, and were best fit with a single component. Most of the observed H_2 arises from $v = 3$, $J = 0$–6, with some H_2 observed in $v = 2$, $J = 0$–3 and a single line observed for $v = 1$, $J = 3$. The broad range of v, J levels observed, and their correlation with Veil component B,

Table 1
Molecular Hydrogen Absorption Features

Transition	WL (A)	EW (mA)	v (km s^{-1})	Log(N)
0–1 P(3)	1166.11	1.01 +/− 0.281	21.4 +/− 0.5	13.10 +/− 0.12
2–2 P(3)	1184.42	1.991 +/− 0.289	19.2 +/− 0.4	12.74 +/− 0.06
1–2 P(0)	1198.00	0.5987 +/− 0.177	18.2 +/− 0.8	11.86 +/− 0.13
1–2 P(1)	1198.48	3.651 +/− 0.357	18.5 +/− 0.2	12.82 +/− 0.04
1–2 P(3)	1202.45	1.892 +/− 0.445	19.7 +/− 0.4	12.60 +/− 0.10
1–2 R(2)	1202.61	1.615 +/− 0.473	20.6 +/− 0.9	12.69 +/− 0.13
1–3 P(2)	1255.38	0.587 +/− 0.096	19.5 +/− 0.2	12.06 +/− 0.07
1–3 P(3)	1257.83	2.09 +/− 0.158	19.2 +/− 0.2	12.61 +/− 0.03
1–3 R(3)	1261.86	1.388 +/− 0.11	19.2 +/− 0.1	12.62 +/− 0.03
1–3 P(5)	1265.66	1.315 +/− 0.166	19.5 +/− 0.3	12.40 +/− 0.06
0–3 R(0)	1274.53	0.3407 +/− 0.141	18.2 +/− 0.9	11.41 +/− 0.19
0–3 P(1)	1274.92	1.815 +/− 0.107	18.8 +/− 0.1	12.32 +/− 0.03
0–3 P(2)	1276.32	0.6608 +/− 0.17	20.2 +/− 0.6	11.93 +/− 0.11
0–3 R(1)	1276.81	0.9871 +/− 0.194	19.9 +/− 0.4	12.35 +/− 0.09
0–3 P(3)	1278.73	2.465 +/− 0.161	19.5 +/− 0.1	12.52 +/− 0.03
0–3 R(2)	1279.46	0.5354 +/− 0.097	19.4 +/− 0.3	12.00 +/− 0.08
0–3 P(4)	1282.14	0.3717 +/− 0.104	20.1 +/− 0.5	11.72 +/− 0.12
0–3 R(3)	1283.11	1.811 +/− 0.145	19.1 +/− 0.2	12.50 +/− 0.03
0–3 P(5)	1286.52	1.575 +/− 0.177	20.7 +/− 0.3	12.36 +/− 0.05
0–3 R(4)	1287.73	0.5645 +/− 0.154	20.5 +/− 0.4	11.97 +/− 0.12
0–3 R(5)	1293.30	1.303 +/− 0.129	19.7 +/− 0.1	12.33 +/− 0.04
0–3 R(6)	1299.81	0.7085 +/− 0.195	20.0 +/− 0.8	12.05 +/− 0.12

Table 2
Carbon UV Absorption Features

Species	WL (A)	EW (mA)	v (km s^{-1})	Log(N)
CI	1260.73	5.598 +/− 0.992	18.2 +/− 0.2	13.02 +/− 0.08
CI	1260.73	3.095 +/− 0.563	23.7 +/− 0.2	12.76 +/− 0.08
CI*	1261.12	2.669 +/− .428	19.2 +/− 0.3	13.11 +/− 0.08
CI*	1261.12	1.194 +/− 0.363	23.7 +/− 0.5	12.76 +/− 0.14
[a]CI**	1277.73	6.82 +/− 0.435	19.5 +/− 0.1	13.45 +/− 0.03
[b]CI**	1329.58	⋯	23.4	12.24 +/− 0.47

Notes.
[a] Single component fit. The abundance for component A, derived in A06, is subtracted out.
[b] Taken from lower S/N data analyzed in A06.

Table 3
$H_2(v, J)$ Column Densities[a]

v, J Level	Log(N)
$v = 1, J = 3$	13.10 +/− 0.12
$v = 2, J = 0$	11.86 +/− 0.13
$v = 2, J = 1$	12.82 +/− 0.04
$v = 2, J = 2$	12.69 +/− 0.13
$v = 2, J = 3$	12.68 +/− 0.07
$v = 3, J = 0$	11.41 +/− 0.19
$v = 3, J = 1$	12.34 +/− 0.06
$v = 3, J = 2$	12.00 +/− 0.09
$v = 3, J = 3$	12.57 +/− 0.03
$v = 3, J = 4$	11.86 +/− 0.12
$v = 3, J = 5$	12.33 +/− 0.04
$v = 3, J = 6$	12.05 +/− 0.12

Note.
[a] When more than one absorption feature corresponded to the same rotational/vibrational level, column densities were obtained by taking average and propagating errors.

will allow us to further constrain the physical properties of the Veil.

The excited state carbon column densities show a significantly smaller abundance of CI** in Veil component A, as shown in Figure 1. A06 measured CI** using an absorption line not observed in the current dataset, with a higher f-value. However, the superior S/N dataset presented in this work was unable to fit multiple components to any of the observed CI** data. The remaining atomic carbon, CI and CI**, clearly show components associated with the two H I 21 cm components.

Overall, the observations point to component B having almost all of the observed H_2 along the line of sight, and having almost all of the CI**. Component B is also hotter, and more likely (van der Werf et al. 2013), closer to the Trapezium. This is somewhat surprising, as one might expect Component A, if it is farther from the Trapezium, to be somewhat more shielded from FUV radiation and therefore have more H_2. However, the location in a PDR where H_2 forms depends on the ratio of the FUV flux to density, and the lower A_V/N(H) ratio toward the trapezium means most of the FUV which is incident upon Component B (again, if it is closer to the ionizing stars) will not be significantly extinguished and therefore also be incident upon component A. A06 found component B to be denser than component A, and also has twice the HI column density. Therefore, if both components have roughly the same FUV radiation (neglecting geometric dilution), then the denser, thicker component should be more efficient at self-shielding.

3. IONIZED LAYERS

In papers A04 and A06 we argued for the presence of a low velocity ionized component in [N II] between θ^1 Ori C and the observer from a single long-slit sample. In this section we

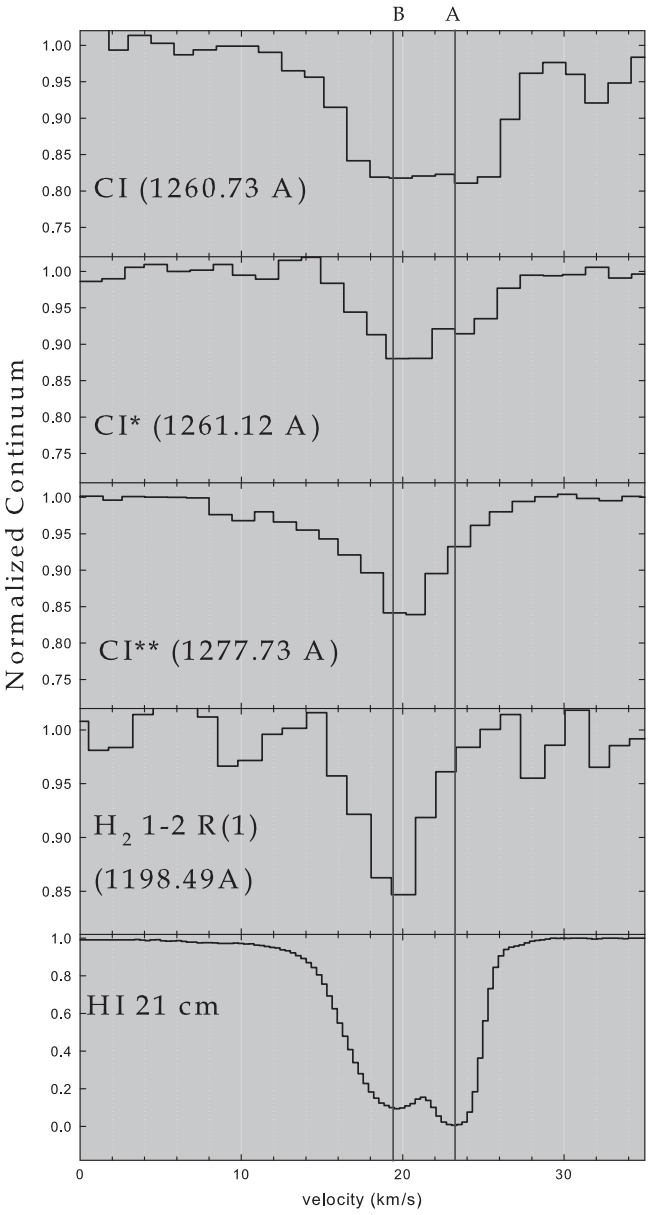

Figure 1. Line profiles for CI, CI*, CI**, H_2, and H I 21 cm. Vertical lines indicate the locations of component A and B. This plot shows that the H_2 and CI** absorption is only seen in component B.

present a much more extensive analysis of radial velocities in the Huygens Region. As in similar past studies (O'Dell 2001) we see that there are both low and high velocity faint components straddling the strong emission arising from the Main Ionization Front (MIF).

We used the compilation of long-slit spectra of Garcia-Diaz et al. (2008) (from multiple sources) in [S II], [O I], [N II], [S III], [O III] and Hα. Typically these spectra were made at 2″ spacing in R.A. and have an instrumental FWHM of about 10 km s^{-1}. In addition, the lines are broadened by small-scale velocity variations and thermal broadening (25.7 km s^{-1} for Hα at 10,000 K, with the thermal component decreasing inversely with the square root of the mass of the emitting ion). What one can see in the spectra is largely determined by the S/N ratio of the spectrum and the observed width of the lines. We made seven samples with a total area of about 40 square arc seconds across regions known to not contain high velocity features in emission from the MIF, which lies on the observer's side of the PDR on the face of the Orion Molecular Cloud (OMC).

Each spectrum was studied using the IRAF task "splot." Initially a Gaussian profile was fit to the strong MIF line. This fit always left unaccounted emission on both the red and blue shoulders of the line. A search was then made for Gaussian profile lines that would account for the emission in the shoulders (a total of three lines, including the strongest). The velocity, flux, and FWHM was recorded for each component. The results for the strongest components (arising from the MIF) are presented in Table 4. They show a trend toward lower radiation velocities with increasing levels of ionization and all of them are at lower velocities than that of the OMC at 27.3 ± 0.3 km s^{-1} as determined from the average of the strong CO lines listed in Table 3.3 VII of Goudis (1982). This trend is what gave rise to the blister nebula model of Zuckerman (1973) and Balick et al. (1974). It should be noted that the same model had been posited by Wurm (1961) on the basis of less commanding data. The [O I] emission arises from exactly at the neutral boundary of the MIF and its value of 25.3 ± 0.7 km s^{-1} suggests a small motion of the ionization boundary relative to the molecular cloud at 27.3 ± 0.3 km s^{-1}.

A detailed presentation of the red and blue velocity component results are given in Section 6.3.2 and interpreted in Section 6.3.3.

4. A RECENT STUDY ARGUING FOR A SMALL SEPARATION OF THE VEIL AND θ^1 ORI C

Recently van der Werf et al. (2013) argued the Veil was only 0.4 pc in the foreground from θ^1 Ori C. This conclusion was based on the properties of a 21 cm absorption feature (their feature F) at −1 km s^{-1} that occurs at an apparent break in Veil Component B. This U shaped feature lies immediately inside the apex of the HH 202 shocks. The 3D structure of HH 202 is well established (O'Dell & Henney 2008), giving a distance along the line of sight of 0.3 pc in front of the Orion-S (where it originates). Assuming a slight displacement of the Orion-S cloud of 0.1 pc in front of θ^1 Ori C, they reached their conclusion of a 0.4 pc separation. The association of Feature F with HH 202 is arguably incorrect, the open end of the U form is pointed toward θ^1 Ori C, rather than along the symmetry axis of HH 202. In addition, the radial velocities in HH 202 range from −38 to −18 km s^{-1} (O'Dell & Henney 2008) while the Feature F velocity only reaches −1 km s^{-1}. In van der Werf et al. (2013), they argue this difference is caused by mass loading and deceleration of the shock. However, the amount of deceleration depends upon many parameters (which are not known from observations) and we cannot judge if the difference in velocities can be used to link the HH 202 shocks and Feature F. This means that the geometric distance derived by van der Werf et al. (2013) is not a constraint to our model.

5. THEORETICAL CALCULATIONS

To determine what the new spectral data tells us about the physical conditions in each Veil component, we have redone the calculations presented in A04. There are several reasons for updating the calculations. For one, Cloudy has undergone significant upgrades in its treatment of PDR physics since the version of Cloudy used in A04 (see Ferland et al. 2013 for a complete review of changes over the last decade). Also, the calculations in A04 assume an H I column density of $10^{21.6}$

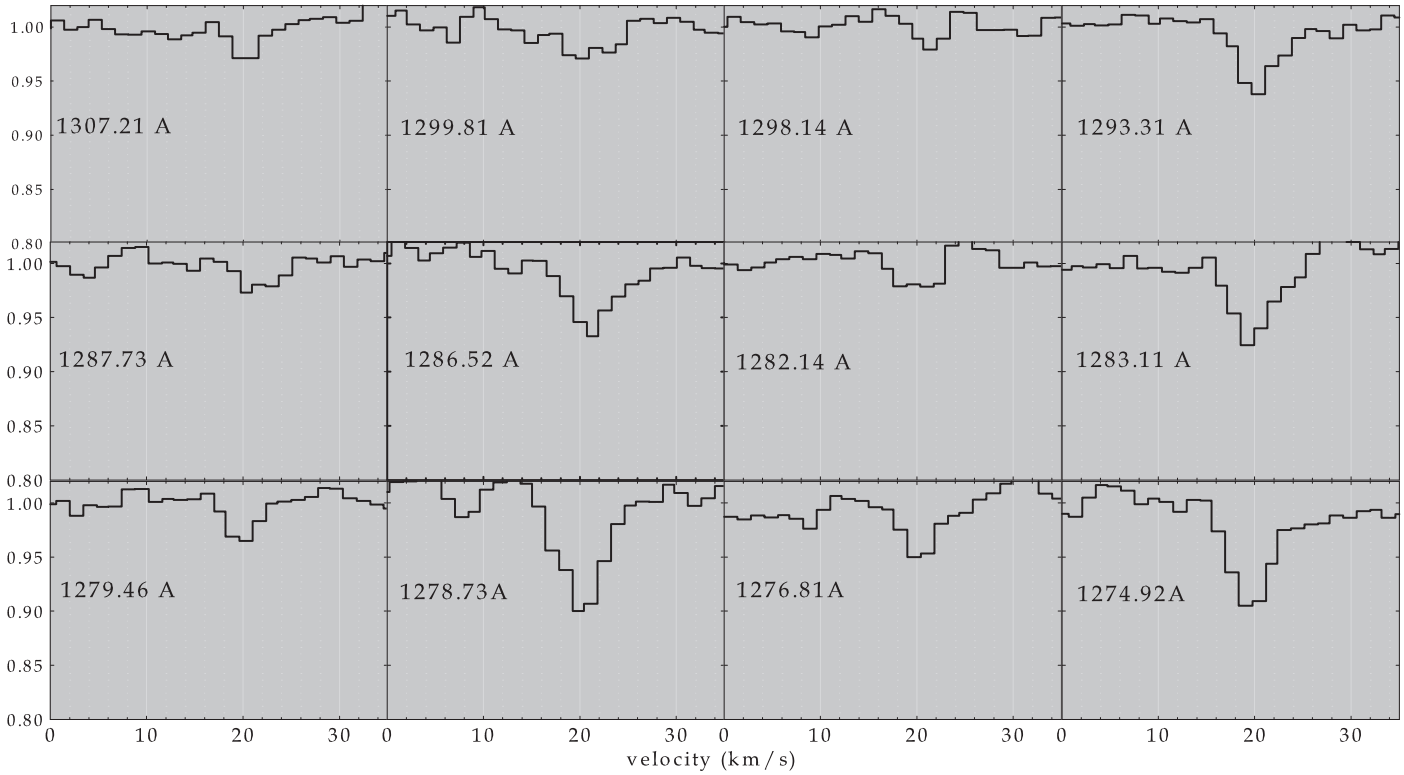

Figure 2. Normalized H_2 line profiles. All profiles show absorption between 18 and 22 km s^{-1}, and associated with component B.

Table 4
Average Radial Velocity[a]

Species	V_{radial} (km s^{-1})
[O I]	25.3 +/− 0.7
[S II]	21.3 +/−1.4
[N II]	19.4 +/− 2.9
[S III]	20.1 +/− 2.9
He I*	19.7 +/− 2
[O III]	18.6 +/− 2.5
Hα	17.3 +/− 1.6

Note.
[a] +/− values represent a combination of the typical error of measurement (about 1 km s^{-1}) and the sample to sample variation (O'Dell et al. 1993).

(derived from Lyα), based on the results of Shuping & Snow (1997). Cartledge et al. (2001), in a STIS UV study of oxygen and krypton abundances toward several sightlines, found an H I column density toward θ^1 Ori B of $10^{21.68\pm0.12}$ cm^{-2}, which agrees with Shuping & Snow (1997) to within the error bars, with a slightly higher mean value. This is the total column density distributed over both components. In A06, we found, for several species expected to be the dominant stage of ionization in H I regions, such as Kr I and O I, that 2/3 of the column density of these species are correlated with Veil component B, and 1/3 in Veil component A. Therefore, we were able to separate out the total H I column densities in each component under the assumption that 2/3 of the total H I column density belongs with component B, and 1/3 with component A. This gives the H I column density in component B as $10^{21.5}$ cm^{-2}, and component A as $10^{21.2}$ cm^{-2}. Since these column densities are different than the column density used in the A04 model, it is prudent to redo the models to account for the new stopping column densities. This is particularly important for the Veil. A04 showed that, due to the Veil's larger than average grain sizes, physical thickness, and close proximity to the Trapezium, that the H_2 in the Veil is not able to self-shield from FUV radiation. However, the H_2 in the Veil is also on a knife's edge, as changing the dust properties, distance, or column density by a small amount would change the predicted H_2 column density by orders of magnitude (see Appendix of A04). Finally, Sofia et al. (2004) have measured the C^+ column density in the Veil, using the 2325 Å line. Since C^+ is the dominant ionization stage in the Veil (the lack of H_2 also means little C^0 or CO), measuring C^+ allows for the determination of the C/H ratio. Taking the Cartledge et al. (2001) value for the H I column density, and the Sofia et al. (2004) value for C^+ gives a C/H ratio of 1.4×10^{-4}, about a factor of two lower than assumed in A04. Finally, given the results of van der Werf et al. (2013) and the potential discrepancy in the Veil-Trapezium distance, it is prudent to revise the models and allow for the possibility that component B is closer than our original estimate.

Overall, using the current version of Cloudy, with a modified stopping criteria reflecting the H I column density in each component, a C/H ratio consistent with observations, and considerations for a closer Veil to Trapezium distance all point to a need to revise the A04 calculations. Our calculations use the latest version of Cloudy, C13, recently reviewed in Ferland et al. (2013). Our calculations follow the logic of the A04 calculations, and so only a brief synopsis is provided here, and we point the reader to A04 for other details.

The geometry of our calculation is one-dimensional, single-sided illumination by a continuum source consistent with the Trapezium cluster. While θ^1 Ori C is the hottest Trapezium star, all four stars A, B, C, and D contribute to the overall UV

radiation field. In addition, the Trapezium stars are known to be multiple star systems, with θ^1 Ori B actually being a five star system. We include a total radiation field consistent with the spectral class of θ^1 Ori A, B, C, and D, along with the binary star companion of θ^1 Ori C. The stellar atmosphere models of Lanz & Hubeny (2003, 2007), along with WM Basic (Pauldrach et al. 2001) were used, with stellar temperatures, masses, luminosities, and surface gravities taken from Table 1 of Ferland et al. (2012). This continuum is consistent with the overall radiation field emitted by the Trapezium, and is very effective in reproducing the spectrum of M42. The total luminosity of this continuum, relative to solar, is $\mathrm{Log}\left[\frac{L}{L_\odot}\right] = 5.35$, with the continuum shape shown in Figure 2 of Ferland et al. (2012). The most important aspect of the radiation field for Components A and B is the flux of FUV, which is parameterized by G_0, with $G_0 = 1$ equal to 1.6×10^{-3} erg cm^{-2} s^{-1}. The flux as a function of distance is shown in several subsequent figures throughout the manuscript. The total Q(H) emitted by all stars in the spectral energy distribution (SED) is $10^{48.8}$ photons s^{-1}. As mentioned below, the Lyman continuum is partially removed to model the ionized component between the neutral Veil layers and the Trapezium. For simplicity, all stars in our choice of SED are assumed to be the same distance away from the Veil. Olivares et al. (2013) in their study of the relative positions of the Trapezium stars find a spatial variation between A–D of 0.025 pc. The Trapezium stars are physically associated with each other, therefore the variation in distance between the stars in the plane of the sky is likely similar to the variation in each stars distance to the Veil. In addition to UV radiation, the other source of ionization are cosmic rays. We use a cosmic ray ionization rate of 2×10^{-16} s^{-1}, based on H_3^+ observations (Indriolo et al. 2007), about ten times higher than that used in A04. Cosmic rays are typically more important in regions with significantly less UV flux than considered in this work, so it is likely our best model for components A and B are not significantly affected by cosmic rays, but we include their effects here for completeness.

It is worth noting that the actual geometry of the Veil environment is more complex than accounted for in our calculations. In reality, the Veil is a three-dimensional entity, with density fluctuations along with anisotropic illumination from all directions. In addition, assuming Component B is closer to the Trapezium than Component A, then Component B will partially shield Component A from FUV radiation. Conversely, Component B is partially shielded from radiation coming in the direction of Earth toward M42, by Component A. To model the effects of Component B on the FUV impingent upon Component A, we constrain the model of Component A to have a G_0 at least a factor of three smaller than the G_0 which strikes the illuminated face of Component B. The factor of three comes from our calculations, as given the grain properties of the Orion environment, and the column density of Component B, the FUV continuum is extinguished by a factor of three by the time it reaches the backside of Component B.

Our calculation is focused on modeling the two H I components observed in 21 cm absorption (A and B). However, there is ionized gas along the line of sight toward the Trapezium, and this ionized gas must lie between the Trapezium and the H I components. A06 reported S III and P III in absorption toward θ^1 Ori B, which provided an estimate to the H^+ column density along the line of sight of 10^{20} cm^{-2}. We account for this component in our calculation by extinguishing the H-ionizing radiation of our stellar radiation field by an absorbing column density of 10^{20} cm^{-2}. This does not remove all of the H-ionizing radiation, and allows for a small H^+ region to form in our calculations at the illuminated face of our simulations. The results of our calculations are insensitive to whether we remove all H-ionizing radiation (a standard PDR calculation assumption) versus only the portion corresponding to the observed H^+ column density, with tests putting the differences to be less than 0.05 dex for CI, CI*, CI**, and H_2. The small differences are the result of the H I region starting at a slightly farther distance away due to the presence of ionized gas, which reduces the UV radiation field slightly via geometric dilution.

All relevant heating/cooling mechanisms are included, such as grain photoelectric heating, H_2 dissociation heating, and cosmic-ray/photoionization heating. Cooling is largely due to PDR fine structure line emission arising from [O I] and [C II]. Cloudy has undergone significant comparisons to other PDR codes under a wide range of conditions (Röllig et al. 2007). Cloudy includes a complete model of the hydrogen atom, which allows us to compute the 21 cm optical depth and compare the $N(H^0)/T_{spin}$ ratio observed in component A and B to our simulation (Pellegrini et al. 2007).

The grain physics package in Cloudy, largely based on the Weingartner & Draine (2001) formalism, is reviewed in van Hoof et al. (2004). Our calculations use a larger than average grain size distribution consistent with the larger value of total-to-selective extinction observed toward the Trapezium ($R_V = 5$, Cardelli et al. 1989). The A_V/N(H) ratio observed toward the Trapezium is 3.3×10^{-22} mag cm^2, and we have scaled the grain abundance to match the observed ratio (A06). Overall, our combined gas and grain abundances lead to half of the carbon being locked up in grains (depletion 0.5). All assumed gas-phase abundances are identical to A04 (which is consistent with the observed abundances in the Orion H II region) with the exception of carbon, which we scaled to match the mean value observed in Sofia et al. (2004).

Three parameters are varied in our calculations, n_H, distance of the illuminated face of each Veil component from the Trapezium (r), and the H I column density $N(H^0)$. We allow the density to vary from $10^{1.0}$ to $10^{6.0}$ cm^{-3}, in increments of 0.1 dex. The Veil-Trapezium distance is varied from $10^{18.0}$ to $10^{19.5}$ cm, also in increments of 0.1 dex. The lower bound allows for the possibility that the Veil is closer than we estimated in A04 and A06, based on van der Werf et al. (2013). All simulations are analyzed at two depths, corresponding to a total H I column density of $10^{21.2}$ and $10^{21.5}$ cm^{-2}, which models the observed H I in each component based on the Lyα derived column density and the ratio of Kr I and O I in each 21 cm component. Since our calculations of the $N(H^0)/T_{spin}$ ratio depend sensitively on the optical depth scale, we compute all density/distance/column density combinations for multiple iterations, until the calculations converge on a solution.

Given the above model parameters, and the high-quality UV and radio data described in Section 2, we are now in an excellent position to understand some fundamental questions regarding the physical properties of each Veil component. Our model results and the consequences of our models on our understanding of the Veil are described in the subsequent sections.

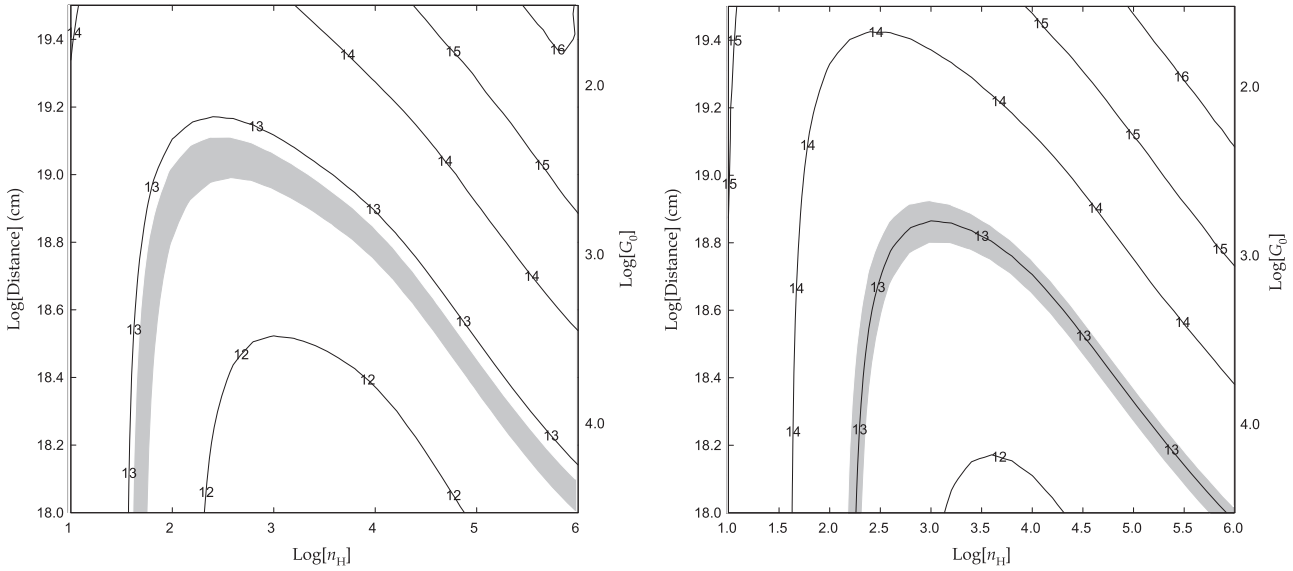

Figure 3. Model results for C^0, $J = 0$ column densities. Contours represent Log[N] for C^0 in the $J = 0$ state. The horizontal axis is the log of the hydrogen density, while the vertical axis gives the log of the distance away from the Trapezium in cm (left side) and the log of the FUV (G_0—right side). Shaded regions represent the 1σ range from this work. For Figures 3–9, the left panel corresponds to Component A and the right panel to Component B.

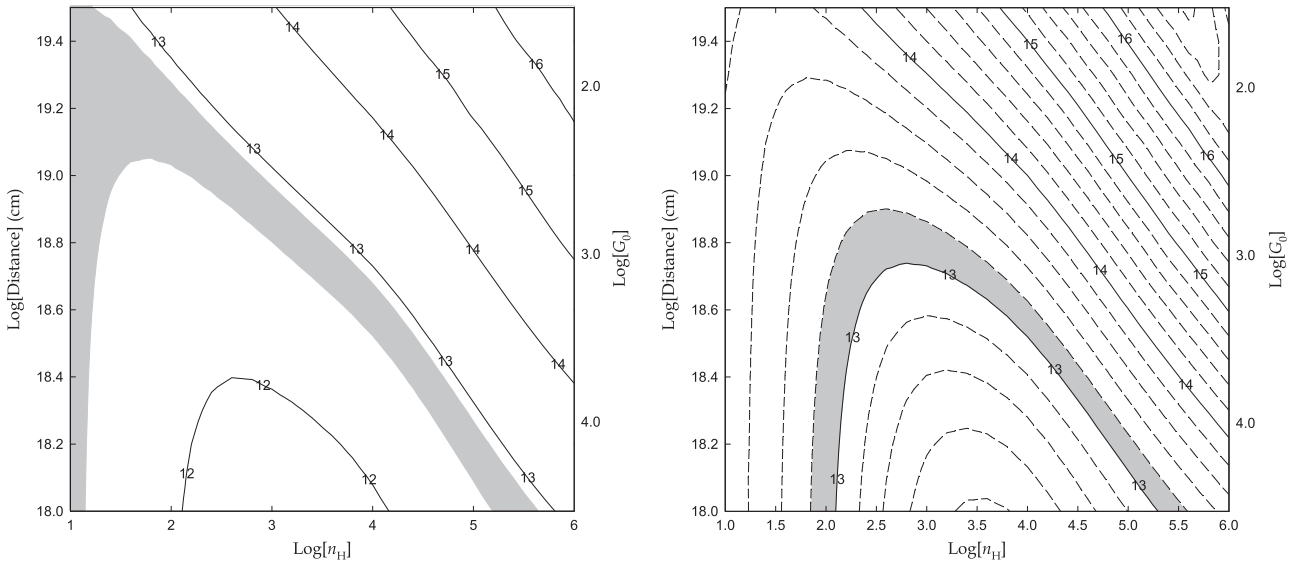

Figure 4. Model results for C^0, $J = 1$ column densities. Contours represent Log[N] for C^0 in the $J = 1$ state. Axes are the same as Figure 3. Shaded regions represent the 1σ range from this work.

6. RESULTS AND DISCUSSION

6.1. Density, Distance, and Temperature for Each Component

Figures 3–5 shows the CI, CI*, and CI** predicted column densities for component A and B, while Figures 6–8 shows the predicted H_2 column density, average H I weighted gas temperature, and predicted ratio of $N(H^0)/T_{spin}$. For each calculation, shaded regions represent the one standard deviation observed range for each observable. For Figures 6 and 7, the gray shaded region represents portions of the parameter space allowed by Copernicus (for H_2) and by the H I 21 cm linewidth (for temperature). Table 5 summarizes the physical conditions for the density/distance calculations that reproduce the observed UV and radio spectrum for each component.

The combination of Figures 3–9, when applied to observations, provides a clear, narrow range of parameter space that reproduces all observables for each component. For component A, the constraint on the temperature and H_2 column density eliminates all densities greater than $10^4\,cm^{-3}$, irrespective of the distance. For densities less than $10^4\,cm^{-3}$, the CI column densities are reproduced, but only for larger distances. In general, models less than $10^4\,cm^{-3}$ are effective at reproducing the observations for a. When we consider the further constraint that Component A has a G_0 at least a factor of three less than the G_0 of Component B (due to extinction) then the best-fit for the distance of Component A from the Trapezium comes out $10^{19.1}$ cm. For that distance, the density that best reproduces the carbon column densities and the $N(H^0)/T_{spin}$ ratio (for a Lyman scaling factor of 0.01, see Figure 10) is $10^{2.4}\,cm^{-3}$. This combination of density/distance corresponds to an average temperature for component A of 50 K, and a FUV flux (relative the interstellar radiation field) of $G_0 = 290$. The best-fit model

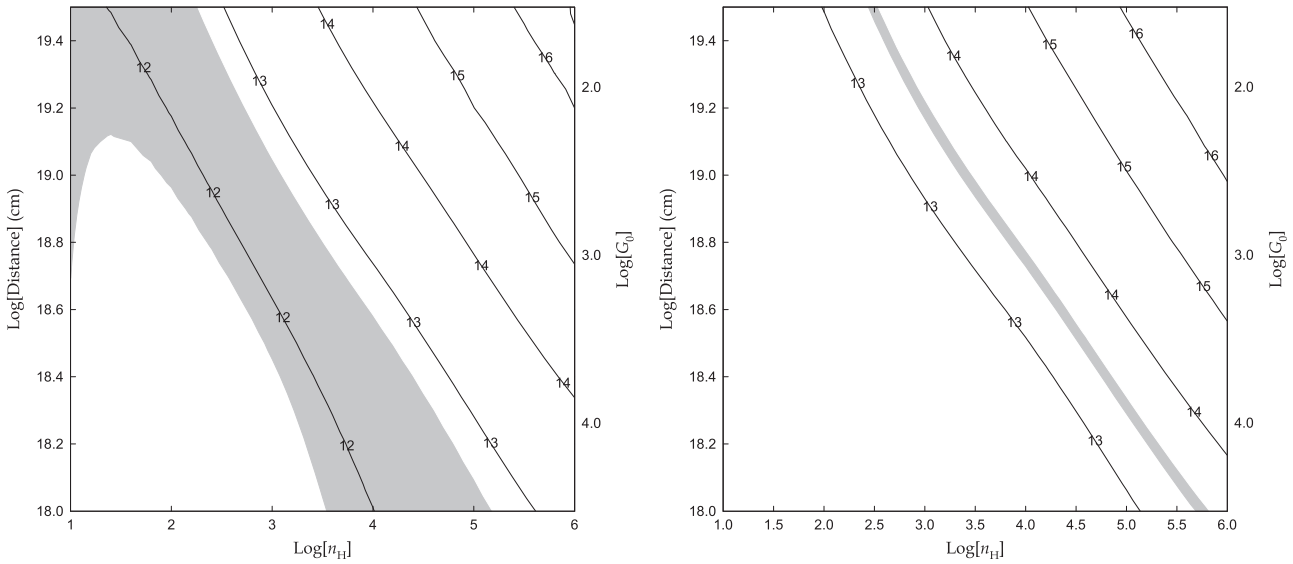

Figure 5. Model results for C^0, $J = 2$ column densities. Contours represent Log[N] for C^0 in the $J = 2$ state. Axes are the same as Figure 3. For component A, observations come from the STIS data analyzed in Abel et al. (2006). Almost all of the CI^{**} is associated with component B, and the low error on the CI^{**} for component B serves as an important constraint in deducing a model.

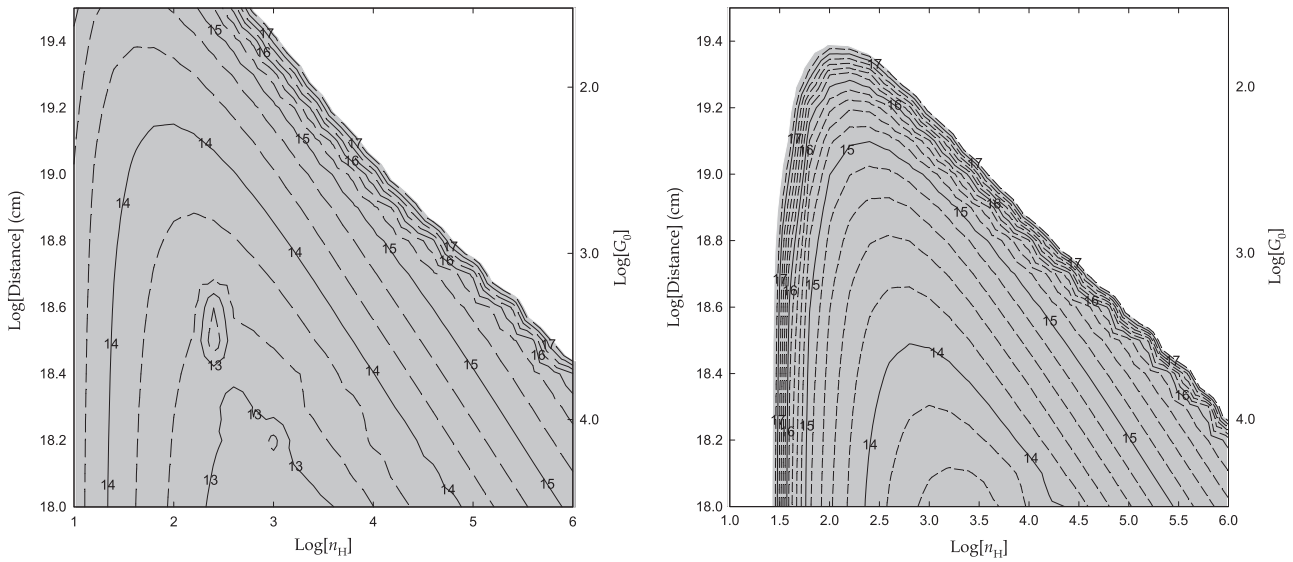

Figure 6. Model results for the total H_2 column densities. Contours represent Log[N] for the total H_2 column density in all v, J levels. Axes are the same as Figure 3. Shaded regions represent the allowed column density based on Copernicus observations.

for component A predicts an H_2 column density (Figure 7(a)) of $10^{14.1}$ cm^{-2}. Figure 9(a) shows, for CI, CI^*, and CI^{**}, the contour line corresponding to where the predictions match the measured column density. This plot shows a small area of intersection at $10^{18.9}$ cm and $10^{2.9}$ cm^{-3}, which has the same G_0/n_H ratio as our best-fit model. However, as we discuss in Section 6.2, the distance we deduce for Component B, based on the H_2 observations, requires a slightly larger distance between Component A and the Trapezium.

The physical conditions derived in this work for component A do not deviate significantly from our previous work (A06). The density derived here is within the range of values given in A06 ($10^{2.1} < n_H < 10^{3.5}$ cm^{-3}), with the use of the H I optical depth allowing for firmer constraints on the density/distance grid. The temperature is also the same as given in A06. The primary difference in our model is we now have a better estimate of the distance and level of UV flux than in previous work. Furthermore, in A06 only an average distance of both components was possible. In this work, we are able to give more precise distances of each component by combining models specific for each H I column density components with the UV data. Finally, the fact we got similar values for both the density and temperature means component A is a region of the ISM whose energetics is still dominated by magnetic fields, therefore a critical conclusion in our previous work is further strengthened by the higher S/N UV data (see Section 6.4).

The observational constraints for component B do not eliminate as much of the density/distance grid, however a narrow range of parameter space that reproduces the carbon and 21 cm data is still clearly shown in the data. The broader linewidth of component B allows for the possibility of this component being both closer and denser than component A. Figure 6(b) shows the Copernicus observational constraint on

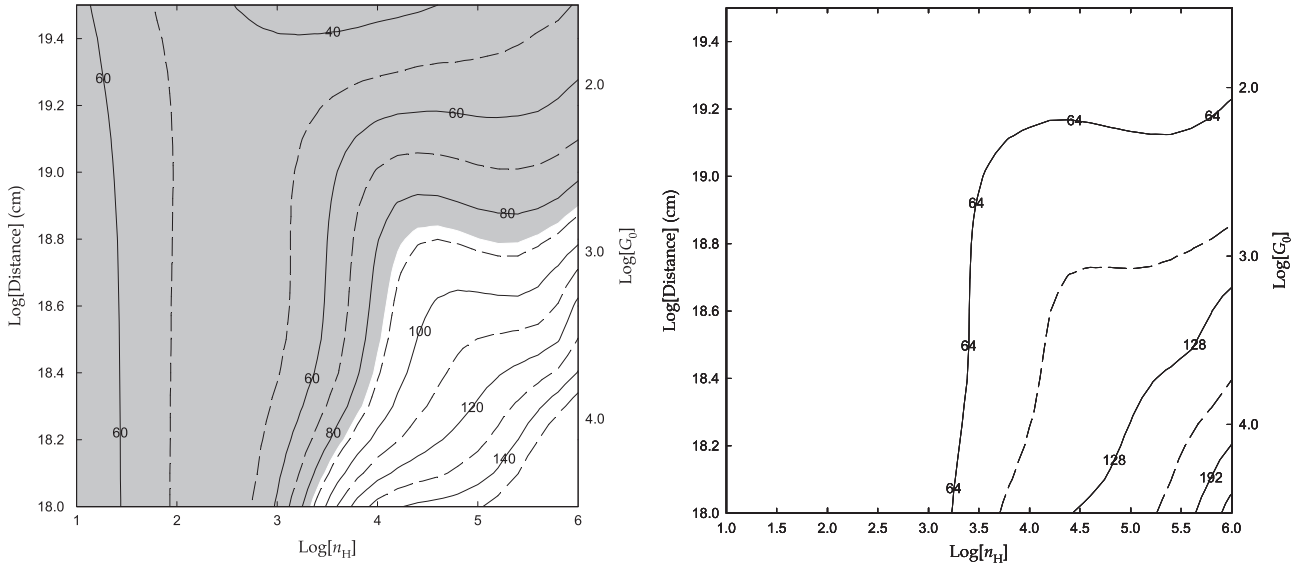

Figure 7. H^0 weighted temperature for each component. Contours represent the temperature. Axes are the same as Figure 3. Shaded regions correspond to temperatures allowed for each component based on the observed HI 21 cm linewidth.

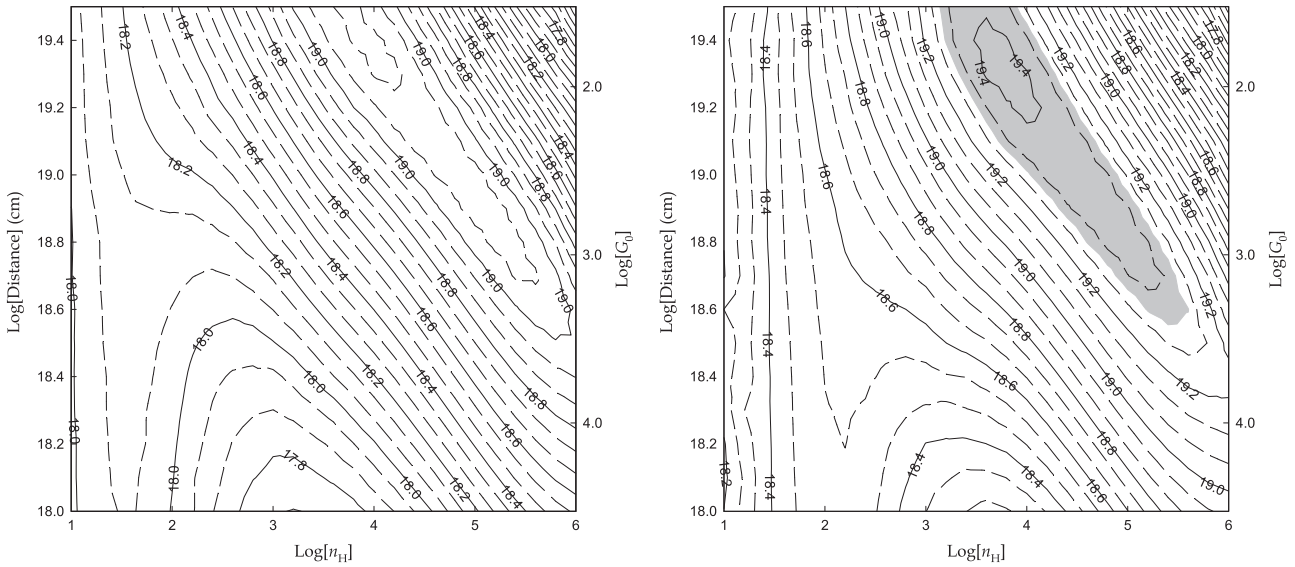

Figure 8. Predicted ratio of $N(H^0)/T_{spin}$. Contours represent Log $[N(H^0)/T_{spin}]$. Axes are the same as Figure 3. Shaded region represents the values determined from 21 cm observations given in A06.

the total H_2 column density again eliminates calculations with larger densities, farther away from the Trapezium (smaller G_0). These models are the ones able to undergo H_2 self-shielding before reaching the total H I column density of $10^{21.5}$ (for component B). Overall, almost half of the parameter space is eliminated by Figure 6(b). The C I column densities for component B start to converge to within two sigma for a distance of $10^{18.8}$ (~2 pc, corresponding to a G_0 of 1000) and densities beyond about $10^{3.2}$ cm^{-3}. Figure 9(b) shows that the CI observations match the models better for increasing density and decreasing distance, until the distance gets to about 10^{18} cm, at which point the CI, and CI* predictions begin to diverge, and the temperature exceeds the maximum limit allowed by the 21 cm linewidth (Figure 7(b)).

One area where our model fails is in the prediction of $N(H^0)/T_{spin}$ (Figure 8). Our best model for Component A predicts this ratio to be 2×10^{18} cm^{-2} K^{-1}, while the Component B model mentioned above predicts 8×10^{18} cm^{-2} K^{-1}. Both are substantially lower than the 1.78×10^{19} and 2.35×10^{19} cm^{-2} K^{-1} measured for each component (A06). This may be due to our choice of stellar continuum. Pellegrini et al. (2007) showed that pumping via Lyman line radiation can significantly decrease the optical depth at 21 cm. Unfortunately, the Veil's obscuration does not allow us to know for certain whether the Trapezium cluster's Lyman lines are in absorption or emission. Therefore, for the best density–distance combination for Component A and B, we computed several models which scaled the strength of the Lyman lines emitted by the stellar continuum, where we allow for the possibility that the Lyman lines in the stellar continuum arriving at the Veil is in absorption or emission. Figure 10 shows how the $N(H^0)/T_{spin}$ varies with the strength of the Lyman lines in the model SED. As expected, decreasing the strength of the Lyman lines increases $N(H^0)/T_{spin}$. At the same time, CI, CI*, and CI**,

Table 5
Best Model Results[a]

Physical Quantity[b]	Component A (Model)	Component A (Observation)	Component B (Model)	Component B (Observation)
N(CI) cm^{-2}	12.88	12.76 +/− 0.08	12.93	13.02 +/− 0.08
N(CI*) cm^{-2}	12.87	12.76 +/− 0.14	13.22	13.11 +/− 0.08
N(CI**) cm^{-2}	12.31	12.24 +/− 0.47	13.07	13.45 +/− 0.03
$N(H_2)_{tot}$ cm^{-2}	14.11	<17.35	14.80	<17.35
$N(H_2)_{v=1,J=3}$ cm^{-2}	12.18	⋯	13.10	13.10 +/− 0.12
$N(H_2)_{v=2,J=0}$ cm^{-2}	10.74	⋯	11.76	11.86 +/− 0.13
$N(H_2)_{v=2,J=1}$ cm^{-2}	11.63	⋯	12.60	12.82 +/− 0.04
$N(H_2)_{v=2,J=2}$ cm^{-2}	11.31	⋯	12.31	12.69 +/− 0.13
$N(H_2)_{v=2,J=3}$ cm^{-2}	10.79	⋯	12.77	12.68 +/− 0.07
$N(H_2)_{v=3,J=0}$ cm^{-2}	10.46	⋯	11.51	11.41 +/− 0.19
$N(H_2)_{v=3,J=1}$ cm^{-2}	11.35	⋯	12.35	12.34 +/− 0.06
$N(H_2)_{v=3,J=2}$ cm^{-2}	11.02	⋯	12.06	12.00 +/− 0.09
$N(H_2)_{v=3,J=3}$ cm^{-2}	11.51	⋯	12.53	12.57 +/− 0.03
$N(H_2)_{v=3,J=4}$ cm^{-2}	11.02	⋯	12.08	11.86 +/− 0.12
$N(H_2)_{v=3,J=5}$ cm^{-2}	11.40	⋯	12.46	12.33 +/− 0.04
$N(H_2)_{v=3,J=6}$ cm^{-2}	10.85	⋯	11.98	12.05 +/− 0.12
$N(H^0)/T_{spin}$ cm^{-2} K^{-1}	9.2×10^{18}	1.78×10^{19}	1.97×10^{19}	2.35×10^{19}
$N(H^0)$ cm^{-2}	1.6×10^{21}	1.6×10^{21}	3.2×10^{21}	3.2×10^{21}
n_H cm^{-3}	$10^{2.4}$	⋯	$10^{3.4}$	⋯
$T_{kinetic}$ (K)	50	<87	60	<320
G_0	290	⋯	800	⋯
Distance to Trapezium (pc)	4.2	⋯	2.0	⋯
Cloud Thickness (pc)	2.1	⋯	0.40	⋯
β_{therm}	0.008	⋯	0.07	⋯
β_{turb}	0.007	⋯	0.4	⋯

Notes.
[a] Best model includes a 0.01 Lyman scaling factor for our SED (see Figure 10).
[b] All column densities are reported in log units.

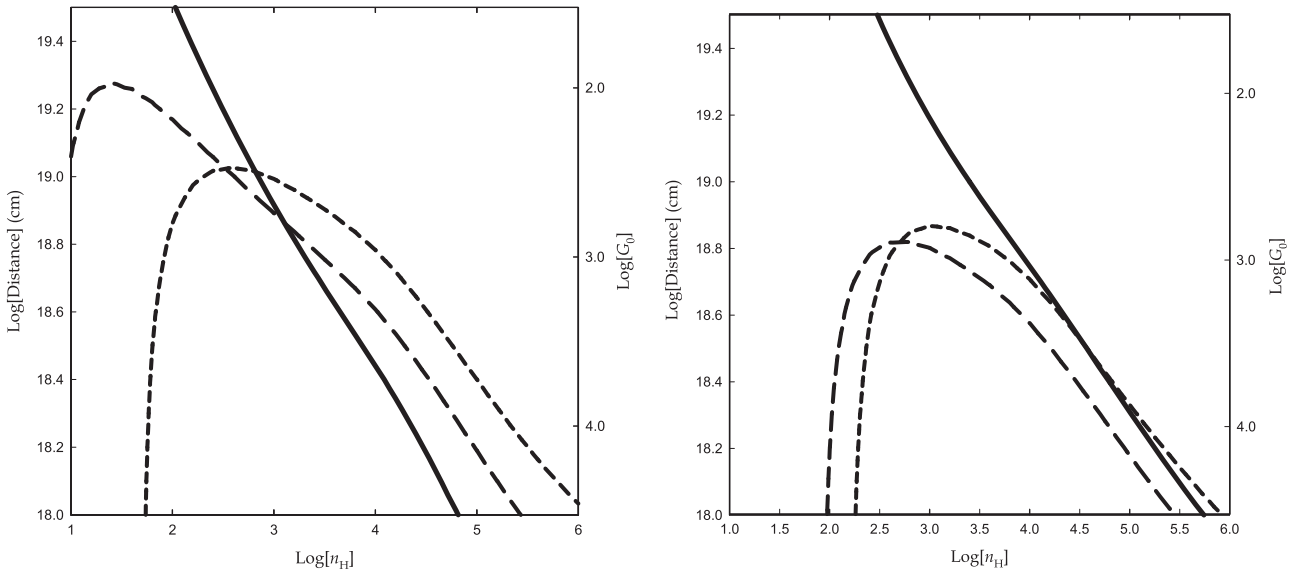

Figure 9. Log of the carbon column densities in the $J = 0$ (short dashes), 1 (long dashes), and 2 (solid line) levels predicted for components A and B. Axes are the same as Figure 3. In this plot, the only contours shown are the ones that match the average observed values for component A and B.

column densities are unaffected, while the H_2 column densities varied by less than 0.1 dex over the four order of magnitude range with which we scaled the Lyman lines. If the stellar continua emitted within the Lyman lines is scaled downward by a factor of 10–100, we can reproduce the radio observations while simultaneously reproducing UV absorption line data (the scaling factors had a negligible effect on the CI and H_2 calculations). Table 5 lists the best fit to the $N(H^0)/T_{spin}$ ratio for each component, with the scaled down Lyman lines.

6.2. H_2

If we had only the CI data, the distance determination from van der Werf et al. (2013) would fit self-consistently in our modeling of Component B, as the 0.4 pc distance fits well with

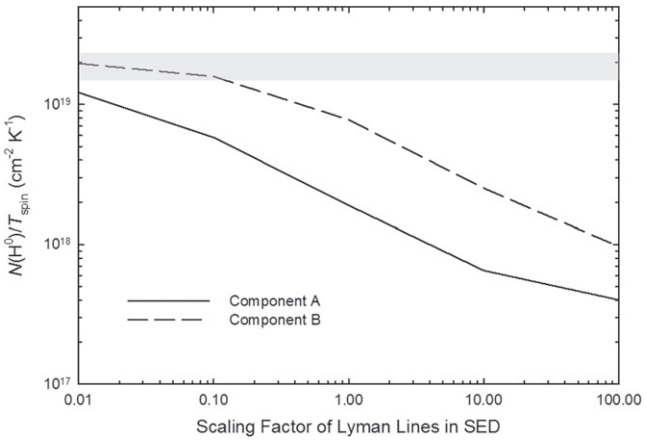

Figure 10. $N(H^0)/T_{spin}$ as a function of the Lyman lines scaling factor applied to our Spectral Energy Distribution, for the best-fit density/distance combination for components A and B. Shaded gray region represents the observed range for the two components.

a high density PDR exposed to a high FUV flux from the Trapezium along with a scaled down continuum in the Lyman lines. The best-fit model for component B predicts an H_2 column density (Figure 6(b)) of $10^{15.1}$ cm^{-2} and a temperature of about 150 K, which is within the range of spin temperatures given in A06. However, since the CI data are sensitive to the combination of density and temperature (thermal pressure—Jenkins 2002) and is not a distance diagnostic, the CI data alone does not exclude the possibility of a larger distance (or lower G_0) and also a lower density.

A better distance constraint for the Veil is possible by combining new H_2 absorption-line observations with theoretical calculations. Studies of H_2 along sightlines toward bright UV are in relatively quiescent regions of the ISM. As a result, the relative column densities serve as an excellent probe of the temperature, density, and other physical properties of the cloud. However, for the Veil, the UV source is not in the distant background, as the Veil is physically associated with the Orion complex. The H_2 level populations are radiatively pumped, making their use as a diagnostic of density and temperature severely mitigated. However, the higher v, J levels are determined by the physics governing UV excitation of H_2. As a result, the distance away (and hence G_0) for each component will be more sensitive to the H_2 level populations, given that the Veil is a region where H_2 is not self-shielded. In the case of the Veil, the geometry allows us to isolate an H^0 region close to a strong UV radiation source. For most PDRs, the geometry probes the entire line of sight, which includes regions that are mostly H^0, H_2, and the $C^+/C^0/CO$ transition. In this case, we are only observing the H^0 region and the transition region from H^0 to H_2.

Figure 11 summarizes our model results for H_2. Figure 11 shows many of the predicted H_2 v, J column densities are in the same range as the observed H_2 column densities. However, just like with the CI observations, there is a degeneracy in the parameter space of density/distance if we just look at the integrated column densities. To break this degeneracy, Figure 12 shows the predicted column density ratio of $N[(H_2)]v = 2; J = 3/N[(H_2)]v = 1; J = 3$, and Figure 13 shows the predicted column density ratio for $N[(H_2)]v = 3; J = 3/N[(H_2)]v = 1; J = 3$. These column density ratios are more sensitive to the excitation of H_2, and thereby the distance of the Veil away from the Trapezium. The observed ratios for Component B are ~0.39 and 0.29. Such ratios are not compatible with the vdW13 distance, unless the density is less than 10^3 cm^{-3}. However, Figure 11 shows densities less than 10^3 cm^{-3} would lead to an order of magnitude disagreement with the CI** and almost all observed H_2 column densities, discrepancies that cannot reconciled by simply scaling the abundances or extinction, since these parameters are already well-known for Orion.

The higher density models allowed by the carbon column densities at the vdW13 distance are not compatible with the H_2 excitation observed in the Veil, providing further evidence for the Veil being significantly farther away than 0.4 pc. It is possible to find a combination of density/distance which fits the UV absorption and HI data for component B. The H_2 and CI data fit reasonably well (both in level of excitation and for total column densities) at a distance of (2 pc) and a density of $10^{3.4}$ cm^{-3}. This is almost identical to the distance/density for Component B derived in A06. The kinetic temperature and Copernicus H_2 constraint all fit within the observed limits. The only inconsistency with the spectroscopic best-fit model is the 21 cm optical depth, which requires a suppression of the Lyman lines in the SED. This distance further constrains the model for Component A, which explains our adoption of a distance of $10^{19.1}$ cm, instead of the intersection point of Figure 9(a) at $10^{18.9}$ cm.

Figure 14 shows the H_2 excitation diagram for the best-model, and for a model which placed Component B at the vdW13 distance and a density of $10^{5.2}$ cm^{-3}, which reproduces reasonably well the CI data observations. Figure 14 shows a comparison between all of the observed H_2 column densities with the best-fit models, and shows more completely what Figure 13 also demonstrates. The H_2 diagram for our best fit model has generally good agreement with observation, reproducing H_2 column densities reasonably well for $v = 1$, 2, and 3. However, the vdW13 distance has significantly more scatter in the predicted H_2 level populations of both models and has trouble reproducing several of the observed column densities to within 0.3–0.4 dex, along with the slope of the excitation diagram. Because this plot depends largely on the excitation physics governing H_2, which in this case is UV radiation, and the UV radiation field intensity depends on distance, this presents a clear demonstration that the vdW13 distance is incompatible with the observed UV absorption spectrum of the Veil.

Given our UV observations, comparison to theoretical calculations, and uncertainty in the underlying assumptions in the vdW13 kinematic distance determination, our conclusion is component B is significantly farther away from the Trapezium than 0.4 pc. Our determination of distances of 2.0 pc for component B, and 4.2 pc for Component A, fit the observed CI and H_2 observations, and agrees with the vdW13 conclusions that component B is closer than component A to the Trapezium. The derived density, combined with the column density, give component B cloud a thickness such that the separation distance between the side of Component A facing the Trapezium, and the side of component B facing Earth, are 1.8 pc apart.

6.3. Ionized Gas Between the Veil and θ^1 Ori C

The presence of low ionization features and H_2 arising from the Veil mean that it must have one or more ionized layers

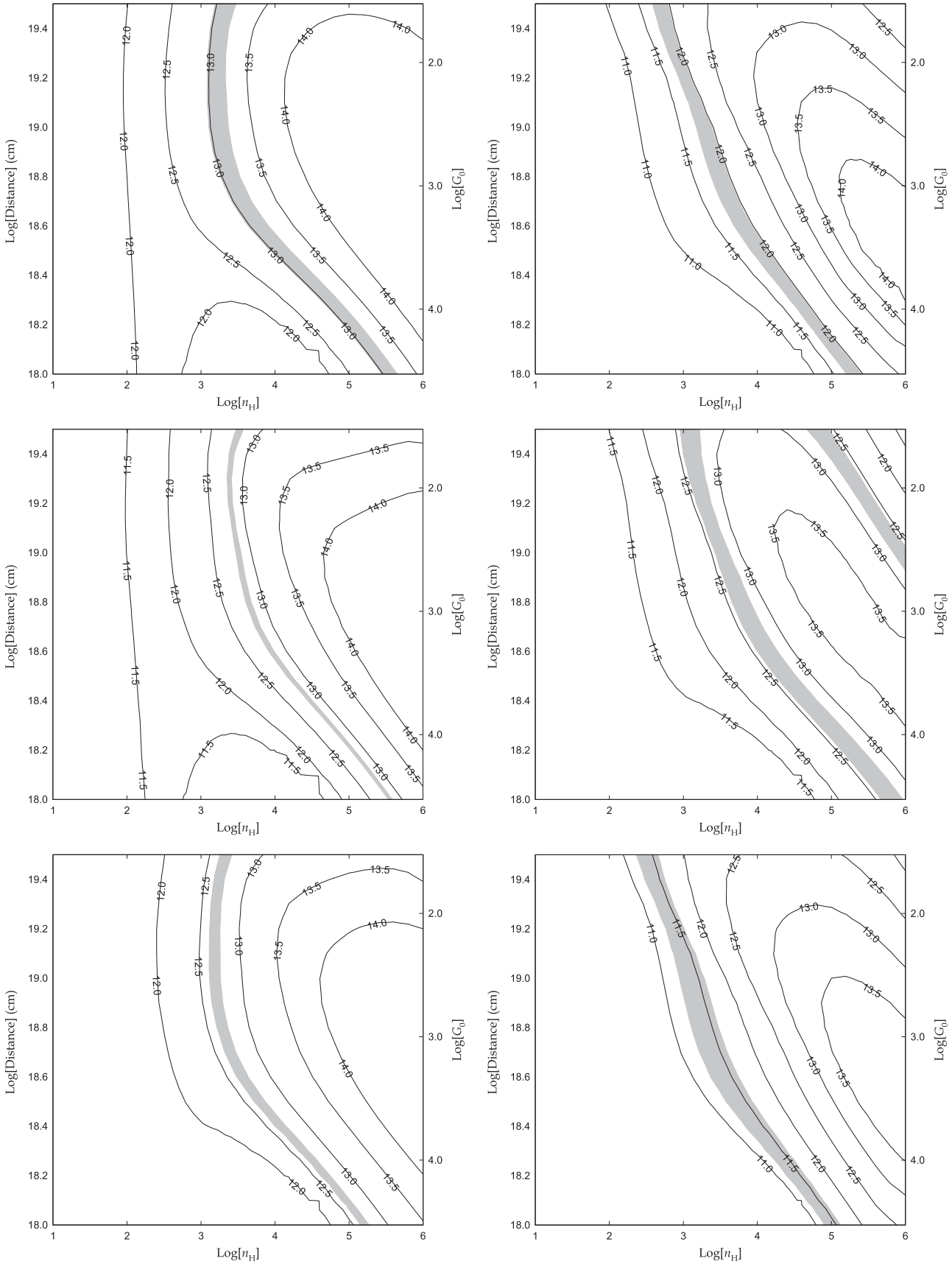

Figure 11. Model results for various v, J H_2 column densities predicted by Cloudy, with the shaded regions denoting the 1σ observed range from the the STIS UV data. Axes are the same as Figure 3. All column densities are for Component B, which is where most of the H_2 is observed. (a) ($v = 1$, $J = 3$) (b) $v = 2$, $J = 0$, (c) $v = 2$, $J = 1$, (d) $v = 2$, $J = 2$, (e) $v = 2$, $J = 3$, (f) $v = 3$, $J = 0$, (g) $v = 3$, $J = 1$, (g) $v = 3$, $J = 2$, (h) $v = 3$, $J = 3$, (i) $v = 3$, $J = 4$, (j) $v = 3$, $J = 5$, (k) $v = 3$, $J = 6$.

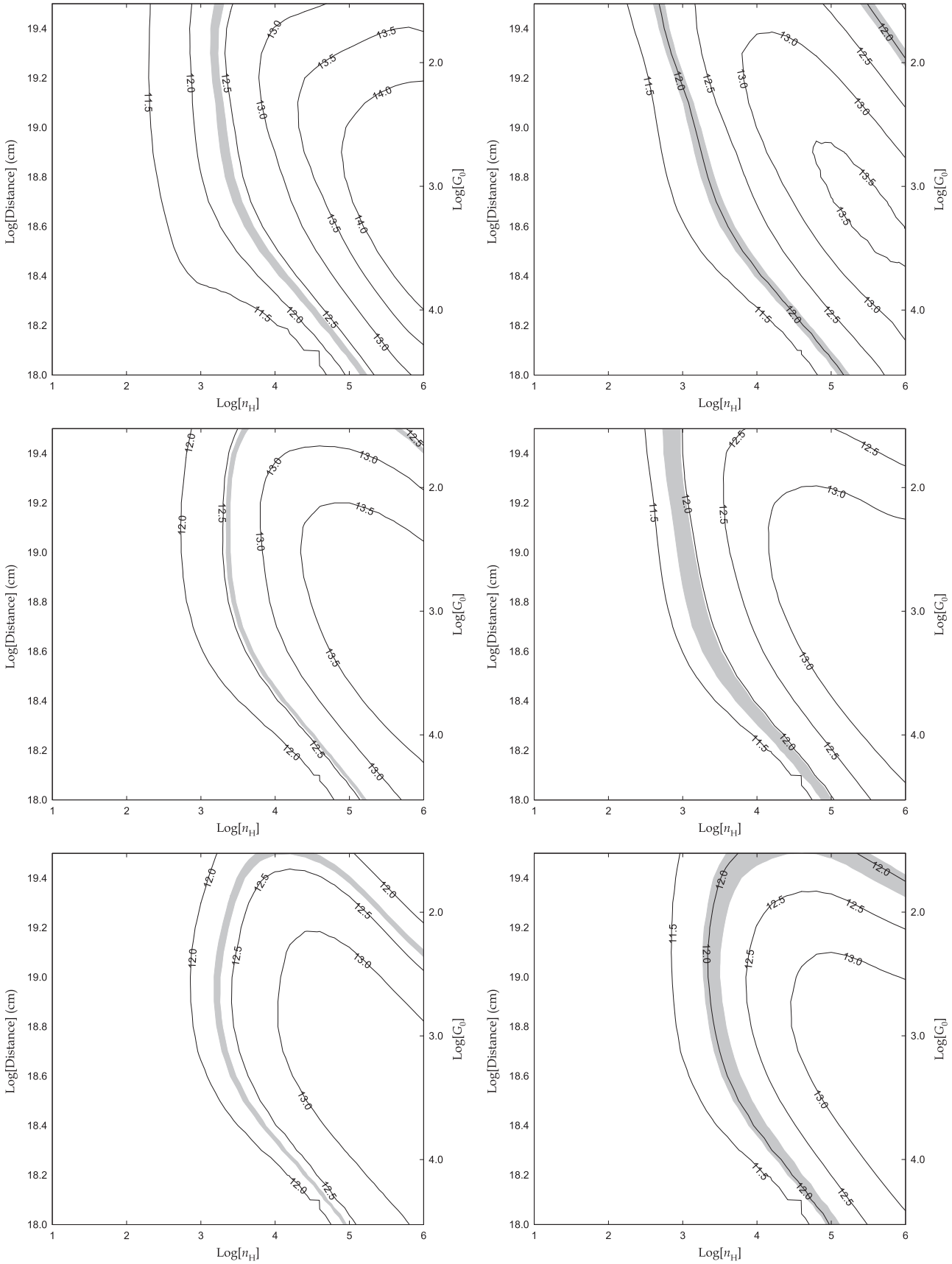

Figure 11. (Continued.)

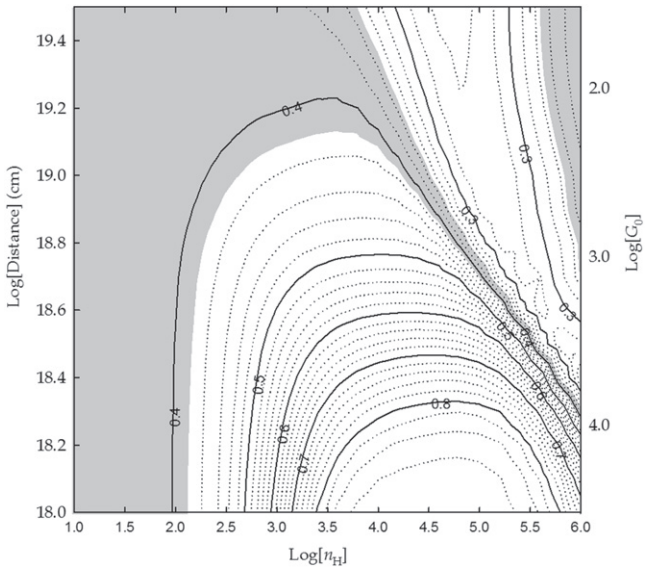

Figure 12. Ratio of $v = 2, J = 3$ column density to $v = 1, J = 3$ column density predicted by our models. Axes are the same as Figure 3. All column density ratios are for Component B.

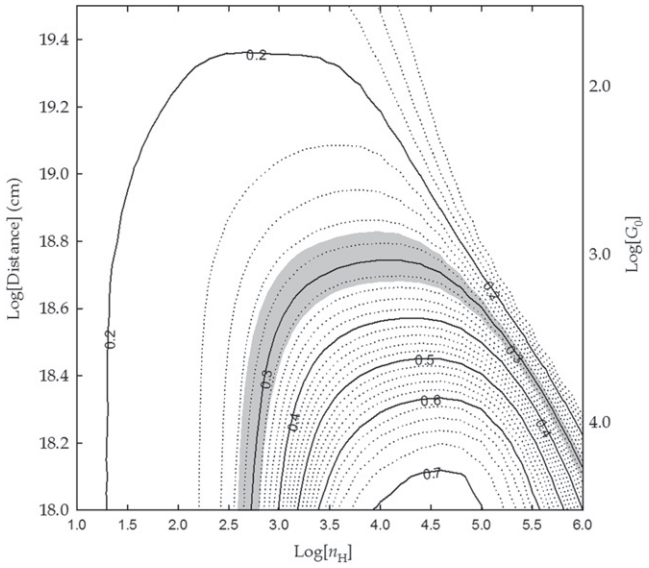

Figure 13. Ratio of $v = 3, J = 3$ column density to $v = 1, J = 3$ column density predicted by our models. Axes are the same as Figure 3. All column density ratios are for Component B.

between it and θ^1 Ori C. In this section we examine the relevance of the red and blue shoulders on the MIF emission lines to the layer(s) between the MIF and the Veil. We first determine if the red component can be due to evaporation from the side of the Veil facing θ^1 Ori C (which it cannot, see below) and then characterize the blue component as it relates to gas between the Veil and θ^1 Ori C.

6.3.1. A Search for Gas Flowing Away From an Ionized Layer of the Veil Facing θ^1 Ori C

Photoionization theory tells us that there must be an ionized zone on the far (toward θ^1 Ori C) side of the Veil. It also tells us that this material will expand away from the Veil and thus would be seen as emission redshifted with respect to the closer (Component B) velocity of 19.4 km s^{-1}.

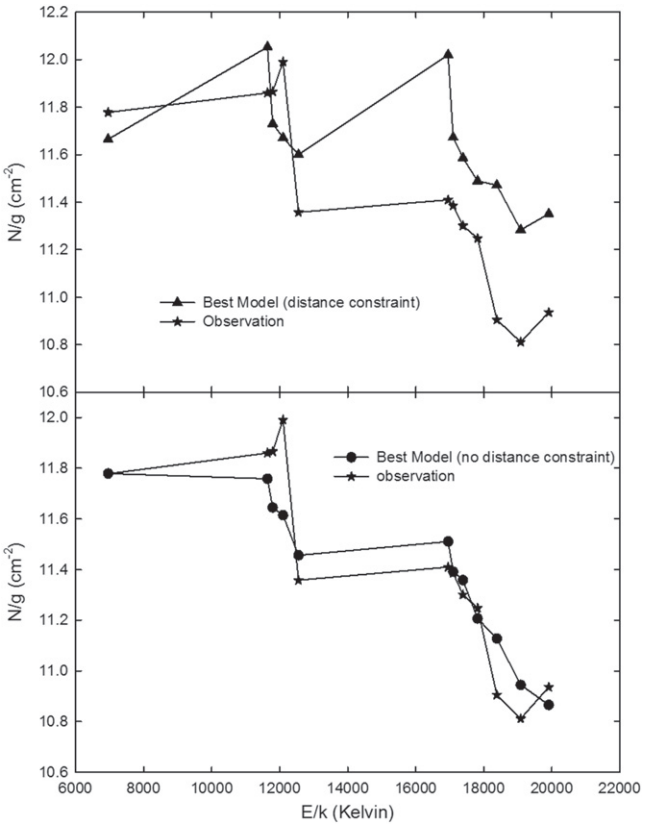

Figure 14. H_2 excitation diagram. The vertical axis is the log of the column density of the absorbing level, divided by the statistical weight, while the horizontal axis gives the excitation energy in Kelvin. The stars represent the observed column densities (divided by the statistical weight for the given v, J, with the circles showing the best-fitting model. The top plot shows the best model for the H_2 excitation, constraining the distance to be less than upper limit given in van der Werf et al. (2013), while the bottom plot shows the best-fit excitation diagram if we remove this distance constraint.

We have conducted a search for that velocity component. If the velocity difference is the same as in the MIF, the values in Table 4 tell us that the [N II] redshifted emission should occur at 27.3 km s^{-1} and the [O III] emission at 28.1 km s^{-1}. Given the narrow region within which the [N II] Veil emission would arise, that emission is better used in searching for its presence along with the emission from the MIF.

There usually are velocity components redshifted with respect to the MIF emission (O'Dell 2001). Our samples used in preparing Table 4 indicate weak (about 10%) [N II] emission at 35.0 $\pm$ 2.4 km s^{-1}, similar to the velocity difference in many spectra of the Huygens Region. These red components have been explained as backscattering by the dust in the PDR beyond the MIF (O'Dell 2001). This is reasonable because the high dust density within the compressed background PDR should be optically thick to visual photons. Because the scattering layer is moving away from the emission layer, the scattered light should be at twice the velocity difference. This means that the average of the velocities of the strong line and the weaker redshifted line should be that of the OMC. The average for [N II] 27.4 $\pm$ 2.5 km s^{-1} and for [O III] 24.6 $\pm$ 2.9 km s^{-1}. This is in agreement, within the probable errors of measuring a weak component on the wing of a stronger line, with the OMC velocity of 27.3 $\pm$ 0.3 km s^{-1}. This is a strong argument that the red shoulder emission almost certainly is due to backscattering. The expectation of there

being strong backscattered radiation comes from the excessively strong continuum of the nebula (Baldwin et al. 1991) that arises from scattered starlight. This is confirmed by a derivation of the distance from the Trapezium stars from the backscattering layer giving the same distance as determined from the surface brightness in hydrogen recombination lines (O'Dell 1994).

As a test of the visibility of [N II] ionized outflow from Component B we constructed a series of artificial spectra. These spectra had two components, both with Gaussian profiles with FWHM = 16.7 km s^{-1}, the average of the MIF [N II] lines and a velocity shift of 6.4 km s^{-1}, the expected velocity difference of the outflow emission. The relative flux in the outflow emission to the MIF emission was varied from 0.0 to 0.4. It was found that "splot" gave velocity differences that were about 13.3 km s^{-1}, that is much larger than the actual secondary line and in this sense comparable to the observed component that we interpret as backscattered light. However, the derived relative fluxes were about 0.02, regardless of the true value. This means that one cannot expect to see direct spectroscopic evidence of putative ionized outflow. However, the observed red component can be attributed to backscattered light, rather than flow away from Component B.

6.3.2. The Blue Component of the Emission Lines

A persistent blue component of the observed [O III] and [N II] lines in the samples used for the preparing Table 4 give averages of 0.9 ± 2.8 km s^{-1} and 1.8 ± 1.9 km s^{-1} respectively. This component was first identified in Section 4.3 of A06 in a single slit spectrum of [N II]. Garcia-Diaz & Henney (2007) summarize the observed characteristics and call it the Southeast Diffuse Blue Layer and report $V = -2$ km s^{-1} in [S II]. It is not seen in [O I], which should arise from immediately at an ionization boundary, whereas [S II] can arise in the helium neutral zone.

There are other features at about the same velocity. The velocities of the P III and S III absorption lines (A06) are $+4.8 \pm 3.0$ km s^{-1} and $+4.5 \pm 0.9$ km s^{-1} respectively. These are comparable to the He I absorption line at 2.1 km s^{-1} and must arise from the same ionized layer. This indicates that there is an ionized layer at about 2.5 ± 2.1 km s^{-1} that lies in the foreground of the Trapezium.

In A06 it was shown that this Blueshifted Ionized Layer must lie between the Veil and θ^1 Ori C because there is insufficient Lyman continuum radiation from the nearest hot star (ι Ori) to cause the observed ionization.

6.3.3. The Distance of the Ionized Layer from θ^1 Ori C

One can estimate the distance between the Blueshifted Ionized Layer and θ^1 Ori C in terms of the θ^1 Ori C—MIF distance (about 0.3 pc). We modeled an ionization layer in the foreground at various distances and present the results for [N II] emission in Figure 15. The results are what one expects, the relative surface brightness of the foreground layer drops approximately as the square of the distance. The ratio of fluxes of the blueshifted and MIF components of the samples we used is 0.08 ± 0.04. This indicates that the Blueshifted Layer is 0.9–1.5 pc from θ^1 Ori C.

This distance is certainly smaller than the distance of 2.0 pc favored by our models. This fact, together with the velocity of the Ionized Layer (1.8 ± 1.9 km s^{-1}) being very different from

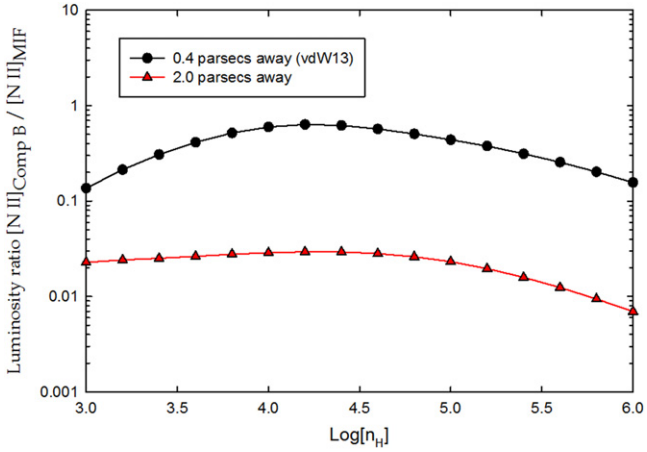

Figure 15. Calculation of the fractional contribution of the [N II] emission arising from a foreground ionized Veil component to the emission from the MIF, as a function of the log of the total hydrogen density. The triangles represent the fractional contribution if Component B (the closer component to the Trapezium) was 2.0 pc away, while the circles are for a distance of 0.4 pc, the limit given in van der Werf et al. (2013).

that expected for a photoevaporative flow from the Veil (6.4 ± 3.0 km s^{-1}) supports the conclusion in A06 that the Ionized Layer is mass limited, rather than having its own ionization front.

6.3.4. Interactions of Veil Components

The relative location of each Veil component relative to the Trapezium couples the radiation field seen by the atomic layers to the radiation field absorbed by the ionized components. The Ionized Layer, between Component B and the Trapezium, will absorb Lyman continuum and FUV photons before reaching Component B. As mentioned in Section 5, we have taken that into account by extinguishing our model SED with a hydrogen column density of 10^{20} cm^{-2}, based on the observed S^{+2} column density and an assumed S/H abundance ratio. In a PDR, the value of G_0 as a function of A_V in large grain environments is approximately $G_0(A_V) = G_{0(\mathrm{initial})}e^{-1.4A_V}$ (Zsargó & Federman 2003). For the column density of the Ionized Layer, and the $A_V/N(\mathrm{H})$ ratio for the Veil of 3.3×10^{-22} mag cm^2, ~95% of the FUV emitted by the Trapezium makes it through the Ionized Layer and encounters Component B. Therefore, the ionized layer has only a minor effect on the FUV and distance deduced for Component B, an effect which our models have taken into consideration.

Since all Veil components (ionized as well as atomic) move relative to one another, future dynamical interactions between the Veil components is likely. In A06, a collision between the atomic Veil components and the Ionized Layer was found to likely occur in about 150,000 years, based on a separation distance between the Veil Ionized Layer of 2 pc. Our current work places the distance between the Ionized Layer and now a specific H I layer, Component B, between 0.5 and 1.1 pc, thereby reducing the time of a collision to between $(3–6) \times 10^4$ years. In addition, since Component A is further away from the Trapezium, the relative velocity of Component A and B means that the two primary H I layers are moving toward each other at a rate of 4.0 km s^{-1}. Our model predicts the back side of Component B (the side facing Earth) is about 2.4 pc away from the Trapezium. This places the separation distance of Components A and B at 1.8 pc. This places the collision time

between the two components at about 1 Myr, much less than the collision time between the Ionized Layer and Component B.

6.4. Magnetic Equipartition

In both A04 and A06, the energetics of the Veil was found to be dominated by its magnetic field. In particular, the multi-component study of A06 found the energetics of Component A was entirely dominated by magnetic fields. The magnetic and turbulent energies for Component B were roughly in equipartition, while the magnetic energy exceeded the thermal energy.

Given the tighter constraints now placed on the density, temperature, and distance of each component, it is important to reassess the state of equipartition for each Veil component. Using Equations (30)–(37) from Heiles & Troland (2005), we computed the ratio of thermal to magnetic energy, $\beta_{\rm therm}$, and the ratio of turbulent to magnetic energy, $\beta_{\rm turb}$. We assume, as in A06, a Helium fraction of 0.1, and $B^2_{\rm tot} = 3B^2_{\rm LOS}$. For Component A, we computed both parameters using $T = 50$ K, $n_{\rm H} = 10^{2.4}$ cm^{-3}, and $B_{\rm LOS} = 46\,\mu$G, where the temperature and density are from the best-fit models from this work and the magnetic field comes from A06. Using these values, we find Component A to have $\beta_{\rm therm} = 0.13$ and $\beta_{\rm turb} = 0.06$. For Component A, both ratios being much less than unity agrees with our earlier conclusion (A06) that Component A is magnetically dominated. For Component B, $\beta_{\rm therm} = 0.07$ and $\beta_{\rm turb} = 0.4$, putting it in rough equipartition, with a slight prevalence toward being magnetically dominated.

7. CONCLUSIONS

1. We have detected over twenty H_2 lines, with high S/N, along with CI, CI*, and CI** absorption lines. We find that almost all of the H_2 arises from Veil component B. Our observations confirm that the H_2 observed is in highly excited v, J levels in line with a region excited by UV radiation, and not collisions. Almost all of the observed H_2 is correlated with Component B, meaning that the component closer to the Veil, and therefore exposed to a stronger UV flux, is more molecular than the farther component A. We suggest this is due to Component B's higher density, which lowers the ratio of flux to density and allows for slightly more shielding at greater depths into the cloud. The back of Component B (the part of the cloud facing Earth rather than the Trapezium) appears to be an HI/H_2 interface that does not fully form H_2 due to running out of material.
2. We have updated our calculations in A04 so that both components are modeled individually. Our calculations, when combined with the UV and radio data, have placed the tightest constraints yet on the density, distance, and UV field strength of each Veil component from the Trapezium, with Component A being largely unchanged from previous work, including the important result that Component A is dominated by magnetic energy.
3. In order to reproduce the observed 21 cm optical depth in each Veil component, we needed to reduce the strength the Lyman lines in the Trapezium, suggesting that the Lyman lines are absorbed before impinging upon the Veil.
4. The H_2 excitation and CI absorption observed in the Component B of the Veil is not compatible with the distance determined in vdW13. A distance of 2.0 pc and density equivalent from A06 reproduces the UV spectrum, but at a distance not allowed by the kinematic constraints observed in Orion. This is not due to our choice of SED, or due to the H^+ layer absorbing FUV along the line of sight. We suggest based on the H_2 spectrum, uncertainties in the kinematic associations of velocity components for the Veil with HH 202, and the lack of H^+ emission, that component B is significantly farther away from the Trapezium than 0.4 pc.
5. We have updated the Cloudy code to include an improved treatment of H_2 formation via chemisorption (Eley–Rideal), which has recently been implemented by the Meudon and KOSMA-τ PDR code.
6. Ionized material redshifted from Veil Component B could not be detected against the MIF emission that is backscattered by dust in the PDR. An Ionized Layer seen in [N II] and [O III] emission along with P III, S III, and He I absorption lies between Component B and θ^1 Ori C.
7. The Ionized Layer of the Veil and Component B should collide within the next 30–60 thousand years, while Components A and B should collide within the next one million years.

This study is based on observations made with the NASA/ESA *Hubble Space Telescope*, obtained at the Space Telescope Science Institute, which is operated by the Association of Universities for Research in Astronomy, Inc., under NASA contract NAS 5-26555. These observations are associated with program #13310. GJF acknowledges support by NSF (1108928, 1109061, and 1412155), NASA (10-ATP10-0053, 10-ADAP10-0073, NNX12AH73G, and ATP13-0153), and STScI (HST-AR-13245,GO-12560, HST-GO-12309, GO-13310.002-A, and HST-AR-13914), and to the Leverhulme Trust for support via the award of a Visiting Professorship at Queen's University Belfast (VP1-2012-025). We would like to thank the referee for a careful reading of this manuscript, and for many useful suggestions.

REFERENCES

Abel, N. P., Brogan, C. L., Ferland, G. J., et al. 2004, ApJ, 609, 247
Abel, N. P., Ferland, G. J., O'Dell, C. R., Shaw, G., & Troland, T. H. 2006, ApJ, 644, 344
Baldwin, J. A., Ferland, G. J., Martin, P. G., et al. 1991, ApJ, 374, 580
Balick, B., Gammon, R. H., & Hjellming, R. M. 1974, PASP, 86, 616
Bohlin, R. C., & Savage, B. D. 1981, ApJ, 249, 109
Cardelli, J. A., Clayton, G. C., & Mathis, J. S. 1989, ApJ, 345, 245
Cartledge, S. I. B., Meyer, D. M., & Lauroesch, J. T. 2001, ApJ, 562, 394
Ferland, G. J., Henney, W. J., O'Dell, C. R., et al. 2012, ApJ, 757, 79
Ferland, G. J., Porter, R. L., van Hoof, P. A. M., et al. 2013, RMxAA, 49, 137
Garcia-Diaz, Ma.-T., & Henney, W. J. 2007, AJ, 133, 952
Garcia-Diaz, Ma.-T., Henney, W. J., Lopez, J. A., & Doi, T. 2008, RMxAA, 44, 181
Goudis, C. 1982, The Orion complex: A Case Study of Interstellar Matter, Vol. 90 (Dordrecht, Netherlands: Reidel)
Heiles, C., & Troland, T. H. 2005, ApJ, 624, 773
Indriolo, N., Geballe, T. R., Oka, T., & McCall, B. J. 2007, ApJ, 671, 1736
Jenkins, E. B. 2002, ApJ, 580, 938
Lanz, T., & Hubeny, I. 2003, ApJS, 146, 417
Lanz, T., & Hubeny, I. 2007, ApJS, 169, 83
Le Bourlot, J., Le Petit, F., Pinto, C., Roueff, E., & Roy, F. 2012, A&A, 541, 76
Lykins, M. L., Troland, T. H., & Abel, N. P. 2010, ApJ, 713, 950
McCandliss, S. R. 2003, PASP, 115, 65
Morton, D. C. 2003, ApJS, 149, 205
O'Dell, C. R. 1994, Ap&SS, 216, 267
O'Dell, C. R. 2001, ARA&A, 39, 99

O'Dell, C. R., & Henney, W. J. 2008, AJ, 136, 1566
O'Dell, C. R., Valk, J. H., Wen, Z., & Meyer, D. M. 1993, ApJL, 403, L678
O'Dell, C. R., & Yusef-Zadeh, F. 2000, AJ, 120, 382
Olivares, J., Sanchez, L. J., Ruelas-Mayorga, A., et al. 2013, AJ, 146, 160
Pauldrach, A. W. A., Hoffmann, T. L., & Lennon, M. 2001, A&A, 375, 161
Pellegrini, E. W., Baldwin, J. A., Brogan, C. L., et al. 2007, ApJ, 658, 1119
Röllig, M., Abel, N. P., Bell, T., et al. 2007, A&A, 467, 187
Röllig, M., Szczerba, R., Ossenkopf, V., & Glück, C. 2013, A&A, 549, 85
Savage, B. D., Bohlin, R. C., Drake, J. F., & Budich, W. 1977, ApJ, 216, 291
Shuping, R. Y., & Snow, T. P. 1997, ApJ, 480, 272
Sofia, U. J., Lauroesch, J. T., Meyer, D. M., & Cartledge, S. I. B. 2004, ApJ, 605, 272
Tody, D. 1993, in ASP Conf. Ser. 52, Astronomical Data Analysis Software and Systems II, IRAF in the Nineties, ed. R. J. Hanisch, R. J. V. Brissenden, & J. Barnes (San Francisco, CA: ASP), 173
van der Werf, P., & Goss, W. M. 1989, A&A, 224, 209
van der Werf, P., Goss, W. M., & O'Dell, C. R. 2013, ApJ, 762, 201
van Hoof, P. A. M., Weingartner, J. C., Martin, P. G., Volk, K., & Ferland, G. J. 2004, MNRAS, 350, 1330
Weingartner, J. C., & Draine, B. T. 2001, ApJS, 134, 263
Welty, D. E., Hobbs, L. M., Lauroesch, J. T., et al. 1999, ApJS, 124, 465
Wurm, K. 1961, ZA, 52, 149
Zsargó, J., & Federman, S. R. 2003, ApJ, 589, 319
Zuckerman, B. 1973, ApJ, 183, 863